Imaging Mechanical Properties of Living Cell by Scanning Probe Microscopy: Tensional Coordination in Cellular Migration

Masafumi NAGAYAMA

Dissertation

December, 2003

Division of Physics, Graduate School of Science,
Hokkaido University

Contents

Chapter 1 Introduction

1.1 Cellular migration

Living creatures consist of cells. Cells are the smallest unit of living matters, which are capable of maintaining its own activities even when they are extracted from its living body. Living activities are accomplished at a cellular level, and then form higher hierarchy levels such as tissues, organs, systems and individuals. Thus, cellular structure and functions give fundamental knowledge to investigate living phenomena. Some kinds of animal cells migrate in living bodies. Cellular migration plays a key role in biological and pathological phenomenon at tissue level such as healing of wounded tissue, self-organizing of the early embryos, immune response, and metastasis of tumor cells. In this section, features of cellular migration are described.

1.1.1 Wound healing in tissue

Cultured cells normally repeat cell division in a petri dish, and then stop proliferating when the dish surface is covered with a cell monolayer. This monolayer is often called “confluent” monolayer. Figure 1.1 shows recovering process of a confluent monolayer after scratching a strip off with glass needle. In the image (A) captured just after scratching, vacant area with width of several hundred μm can be seen. 8 h later, cells remaining at the margins of the vacant “wounded” area extend toward wound (*arrows* in (B)). On the other hand, cells far from the wounded area do not change its shape and not migrate. In the image (C), cells migrate into the wounded area, and some of them divide. 24 h later, although the wound part is almost covered with cells, migrating cells looks larger than stationary ones (D). Subsequently, the cells becomes smaller according to repeating cell division. It continues until confluent monolayer is re-formed ((E) and (F)). Then, the monolayer is maintained. This result suggests that cells in a tissue have some mechanism which senses defects of a tissue, and controls own migration and division to recover its original form. The similar phenomenon is observed also in a tissue such as a skin in living body. Regulation of cellular migration is essential to homeostasis on normal tissue.

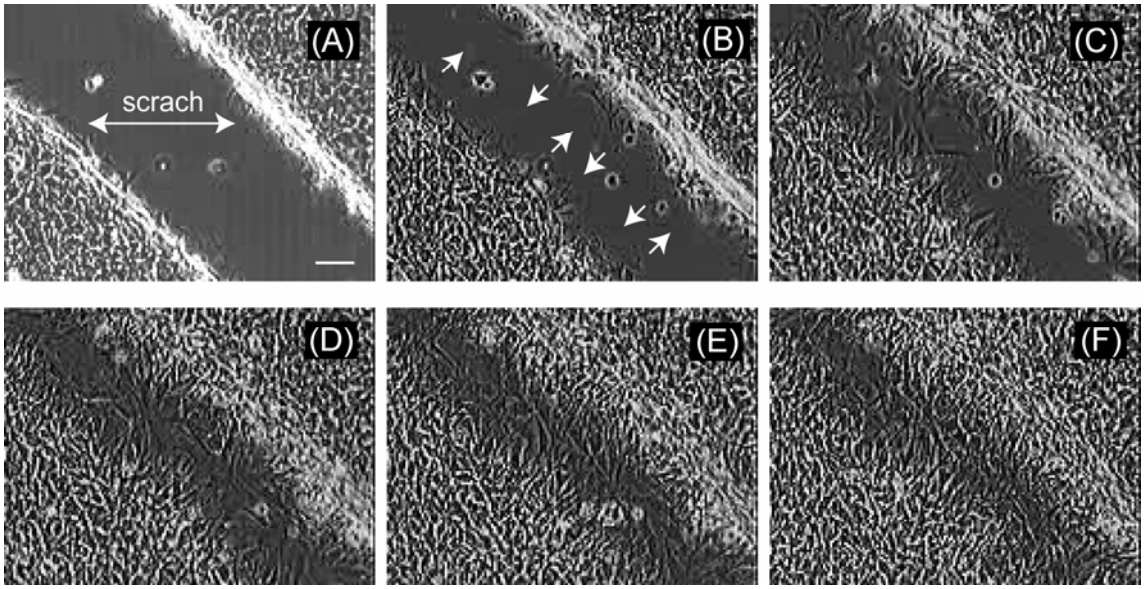

Figure 1.1 Time-lapse images of cultured fibroblasts recovering a cell monolayer. These images are obtained with phase contrast microscope at 8 hours intervals. Scale bar, 100 μm. (Courtesy of Mr. Takeomi Mizutani)

1.1.2 Phagocytosis of neutrophil

Immune response is another example of cellular migration in living body. A neutrophil, which is a kind of leukocyte, has an ability to chase and eat bacteria invaded from outside of a living body. This action is called phagocytosis. This saves living body from certain death by infection. Figure 1.2 shows the time-lapse images of a neutrophil chasing a bacterium. These sequential images are taken from a 16 mm movie made in the 1950s by Rogers at Vanderbilt University [1]. A neutrophil on a blood film is chasing a bacterium (*arrow-head*) like a cat chasing a mouse, pushing aside red blood cells. Crawling neutrophil has a characteristic asymmetric shape with fan-shape lamella in an anterior portion and a narrow tail in a posterior portion. The lamella is elongated toward an objective continuously, varying direction of elongation (*arrow* in (C) and (G)). As the tail is dragged, the neutrophil migrates in the direction of lamella elongation, changing its shape. Finally, the neutrophil catches the bacterium and engulfs it. This experiment suggests that a single cell controls its migration and shape, according to the outside environment even if it is not in a tissue. However, the cell has no specific

sensory and locomotory organelle such as eye and foot. Mechanism which induces such a cellular migration has not clarified yet.

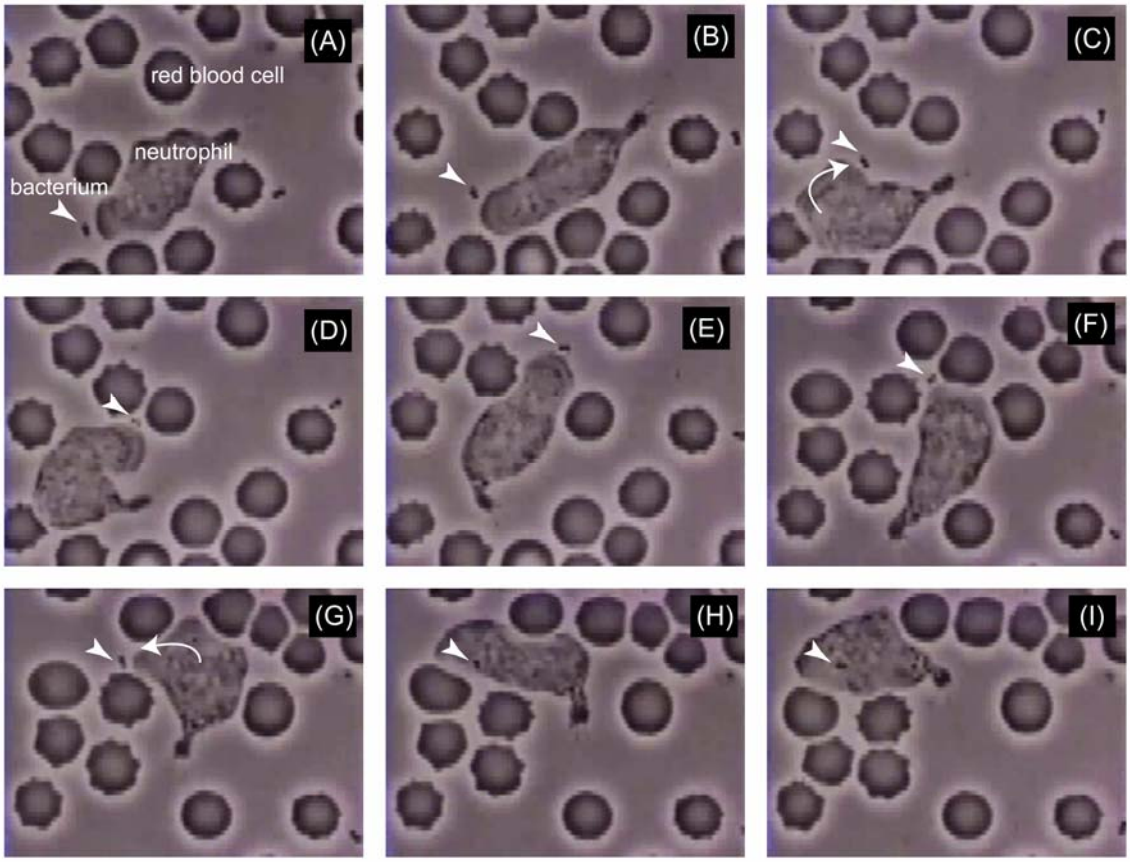

Figure 1.2 Phagocytosis of neutrophil. A neutrophil is chasing a bacterium (*arrow-head*), pushing aside red blood cells. Finally, the neutrophil engulfs the bacterium (H). [1]

1.1.3 Time-lapse observation on cultured fibroblasts

Features of cellular migration are examined in detail by time-lapse images of cultured fibroblasts in Figure 1.3. In the case, there is no specific stimulus such as wound or bacterium. Just after scattered on surface of a petri dish, fibroblasts still drift in water and have a spherical shape with diameter of about 20 μm (*white arrow-heads*). Probably, this shape originates in isotropic osmotic pressure exerted on the cell from surrounding medium. When fibroblasts contact surface of a petri dish physically, they begin to spread thinly on the surface. Some fibroblasts already begin to spread in the

image of 0 h (*black arrow-heads*). In fact, taking account of the time required for the setting to experimental equipment, it is found that fibroblasts have the ability to start spreading within 10 min after contact. Fibroblasts have round shape initially and become slender shape gradually (*black arrows* in 0.5 h). The slender fibroblasts start to migrate along their long axis. When fibroblasts change its polarity, they change direction of the migration (*black arrow* in 6 h). Repeating migration along its long axis and change in its direction accompanying shape change, fibroblasts crawl on the surface of a petri dish. *Dashed arrows* in the image of 10 h indicate moving tracks of the center points about five fibroblasts selected randomly. Under no specific stimulus, fibroblasts seem to migrate with no correlation in respect to its direction and speed. Nevertheless, there is no difference essential in repeating alternately two phases, which are linear migration and its direction change, during cellular migration. The two phases composing cellular migration are described below in detail.

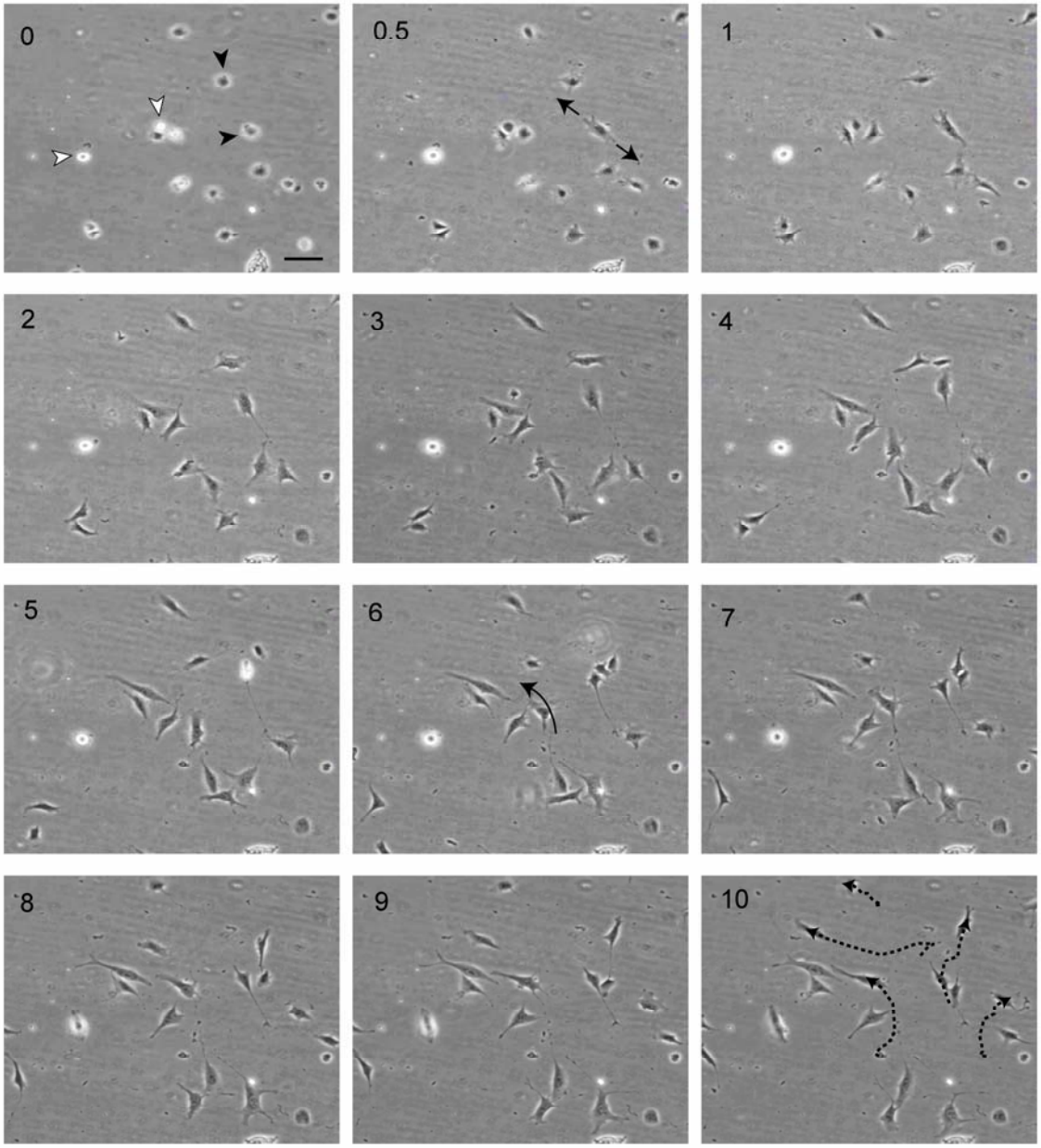

Figure 1.3 Time-lapse phase contrast images of cultured fibroblasts in the case of no specific stimulus. Time in hours is indicated. Scale bar, 100 μm.

Linear migration

Three fibroblasts migrate linearly along the direction of its long axis, which is indicated with *white arrows* in Figure 1.4. Each image is captured every 1 hour with an optical microscope. A fibroblast has a sheet-like structure at one end of its slender shape.

The sheet-like structure and its edge are referred as “lamellipodium” and “leading edge”, respectively. On the other hand, the fibroblast forms a narrow tail at the opposite end. To migrate linearly, a fibroblast initially extends the lamellipodium in the direction of migration (*filled arrow-heads*), and then drags its cell body forward, retracting the tail (*open arrow-heads*). Thus, the slender shape including the difference in the structure at both ends decides the direction of cellular migration, that is, it represents cellular polarity. *Dashed arrows* in the image (F) indicate moving tracks of the center points about each fibroblast. The moving tracks are almost linear throughout this observation. Average speed of migration is about 20 μm/h.

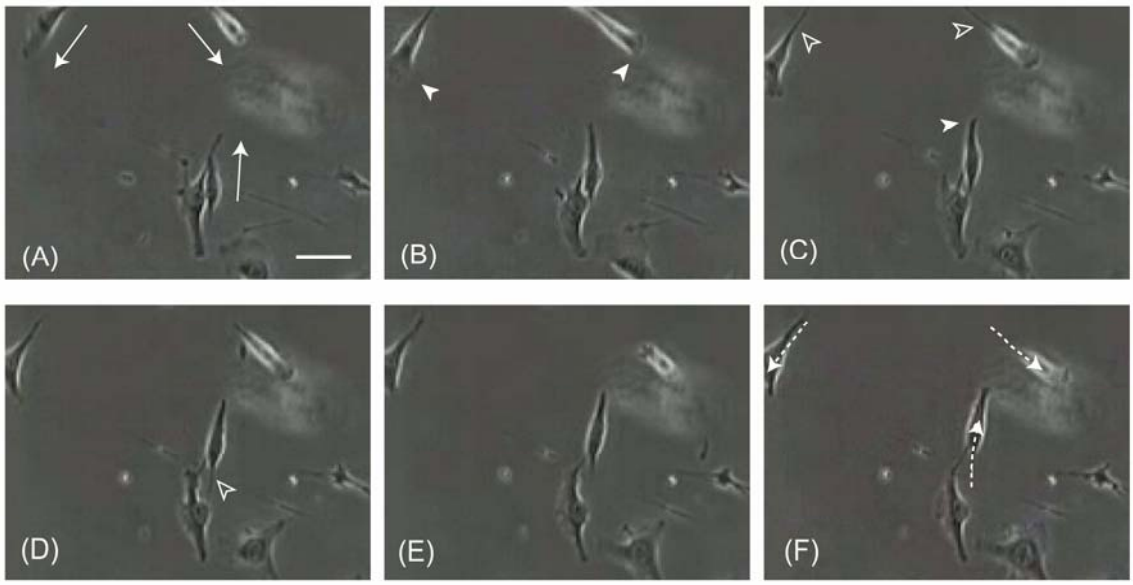

Figure 1.4 Linear migration of fibroblasts on glass substratum. Images are taken at 1 hour intervals with phase contrast microscope. Scale bar, 100 μm.

Direction change

Figure 1.5 shows a fibroblast changing direction of migration. Each image is captured every 50 minutes with optical microscope. In the image (A), a fibroblast is highly polarized in the direction indicated with an *arrow*. The fibroblast migrates downward in the image, retracting its tail (*open arrow-head* in (A)), and then new lamellipodium (*filled arrow-head* in (B)) extends from the side portion of the slender shape. The opposite end to new lamellipodium is changed to tail-like structure (*open arrow-head* in (C)), and then it retracts. In the time course of images (D) through (I),

two lamellipodium extend in the other direction in sequence (*filled arrow-heads* in (D) and (F)). At this time, the fibroblast does not have any longer one-dimensional slender shape, but the shape elongating protrusions in the multiple directions. Although the tail becomes narrow according to dragging cell body, it remains without retracting completely (*open arrow-head* in (G)). *Dashed arrow* in the image (I) indicates moving track of the center points. The fibroblast migrates unsteadily, changing its direction whenever new lamellipodium extends. From this experiment, it is found that fibroblasts extend new lamellipodia in another direction to determine the next direction of cellular migration.

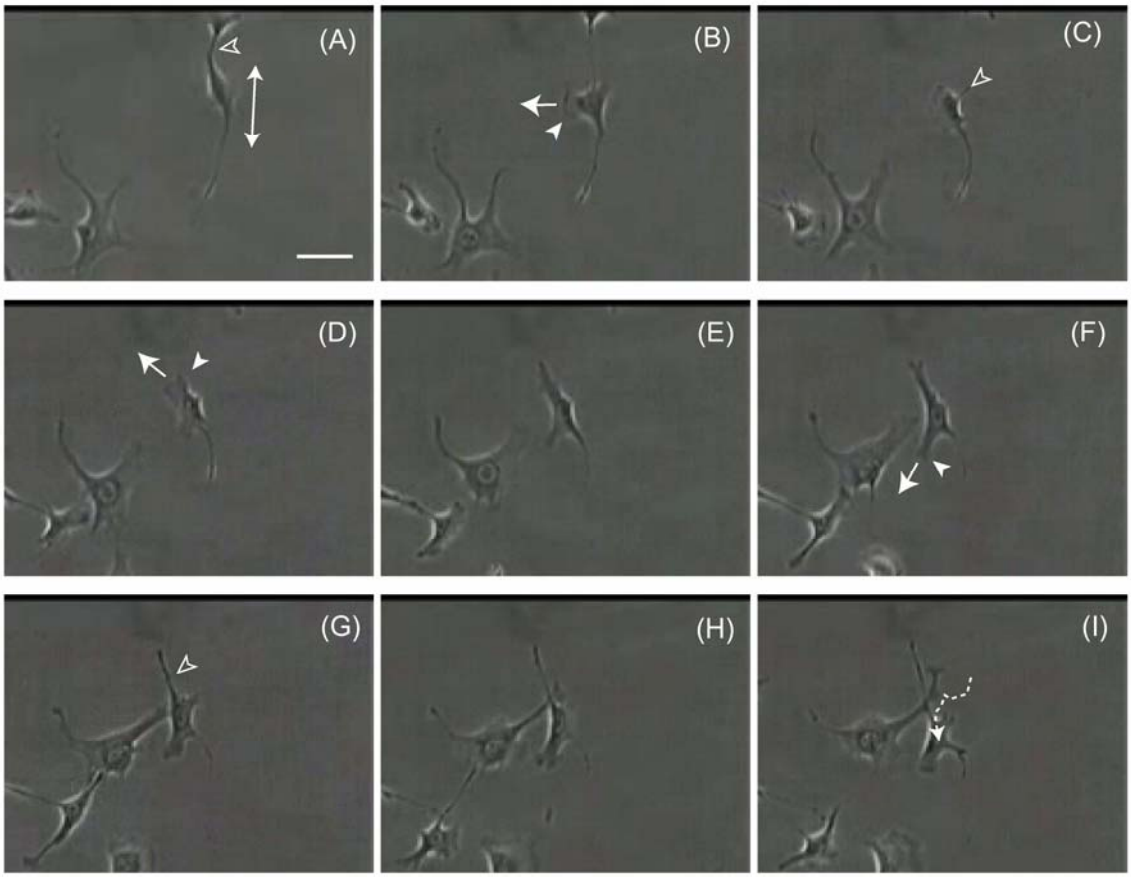

Figure 1.5 Time-lapse images of a fibroblast changing direction of its migration. Images are taken at 50 minutes intervals with phase contrast microscope. Scale bar, 100 μm.

The procedure of cellular migration is shown in Figure 1.6(A) as schematic drawings. Fibroblasts which have one-dimensional slender shape migrate linearly

according to continuous extension of a lamellipodium. When new lamellipodium begins to extend from side portion of a fibroblast, the fibroblast changes own shape and stops migrating linearly. Subsequently, when the new lamellipodium continues to extend, the fibroblast obtains again the slender shape and starts migrating linearly. Figure 1.6(B) shows moving track of a fibroblast measured under culture condition for 48 hours. The initial and final positions are indicated with S and F, respectively. This fibroblast migrates along the *arrows* indicated in this Figure, changing its direction drastically several times, and finally reaches the position of F. The fibroblast stays for a long time in the region indicated with ①, whereas migrates linearly for a long time in the region indicated with ②. In other regions, the fibroblast migrates unsteadily, changing its direction frequently. In the case of no specific stimulus, the moving track seems to be similar to that of Brownian motion. The random migration may originate in response of the fibroblast to random stimulus, which is a local density fluctuation of chemicals in medium or a convection of medium. When fibroblasts receive a stimulus from a specific direction, they start migrating linearly toward a target, as shown in Figure 1.1. It is expected that extracellular stimuli switch migration of fibroblasts between linear migration and direction change.

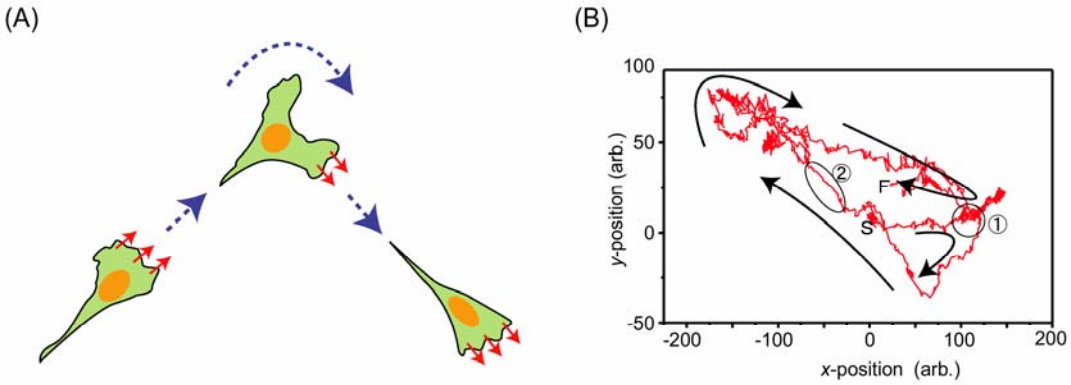

Figure 1.6 (A) Schematic drawings of cellular migration. A fibroblast migrating linearly has one-dimensional slender shape. When the fibroblast changes direction of its migration, it changes its own shape extending new lamellipodium. (B) Moving track of fibroblast for 48 hours. S and F indicate initial and final positions, respectively.

Focusing on a procedure of cellular migration with a shorter time scale, one step of cellular migration can be separated roughly into two local processes: extension of

lamellipodium and retraction of tail. Figure 1.7 shows the one step of migration schematically. When a cell starts on migration, a lamellipodium is extended forward (A). The extended lamellipodium is attached to substratum; a tail at posterior portion is detached from substratum (B). The detached tail is retracted toward cell body (C). By one cycle of extension and retraction, center of mass of a cell migrates one step. By repeating such one step of migration, cells migrate occasionally changing a direction according to extracellular stimulus. In case of fibroblasts, a few 10 μm migration is accomplished in several 10 min as one step migration. Although one step of their migration has different temporal and/or spatial scales, the manner of migration is common to adhesive animal cells. Studies on one step of migration are fundamental and important to understand mechanism of cellular migration.

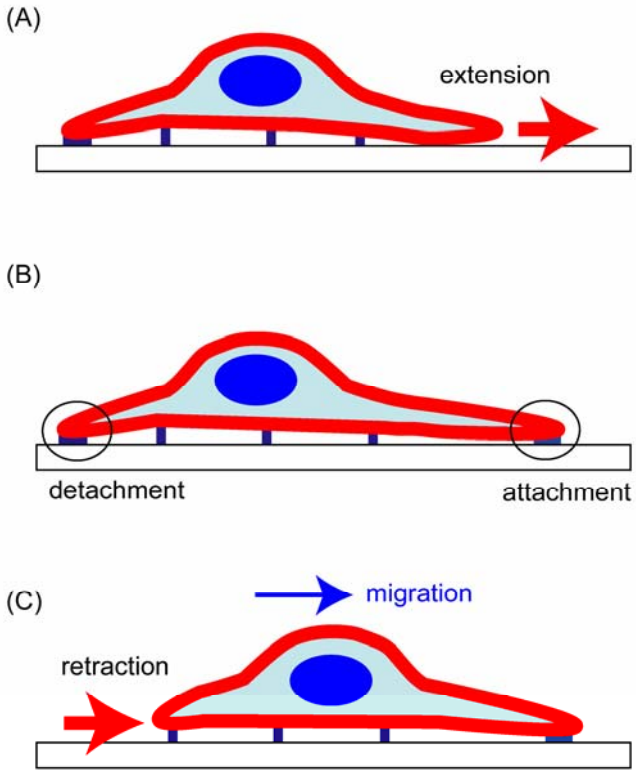

Figure 1.7 Schematic drawings of one step of cellular migration. (A) Lamellipodium extension. (B) Attachment of lamellipodium to substratum and detachment of tail from substratum. (C) Tail retraction.

1.2 Studies on mechanism of cellular migration

Cellular migration has been widely studied in interdisciplines. Various kinds of phenomena on different scale are focused on, as shown in Figure 1.8. In biochemistry and molecular biology, many proteins related to cellular migration are identified along with corresponding gene sequence, and these structures and functions are intensively investigated. In biophysics and cell biology, it is investigated how related proteins interact with each other in a cell and performs its function to induce cellular migration. However, cellular migration is one of the most difficult subjects to explain at the molecular level because different portions of a single cell change simultaneously on macroscopic scale. To induce cellular migration in a given direction, numerous proteins must be coordinated both spatially and temporally throughout the cell. In mathematics and statistics, moving tracks of cellular migration are analyzed theoretically to examine universal features [2]. However, experimental support to these studies has not been discussed yet. Thus, understanding cellular migration as an integrated process requires an experimental investigation of mechanical properties of multicomponent structures [3, 4]. Recently some researchers begin to study mechanical properties of living cells from this viewpoint.

In this section, studies on a mechanism of cellular migration focused on cytoskeleton are described from both biomolecular and mechanical points.

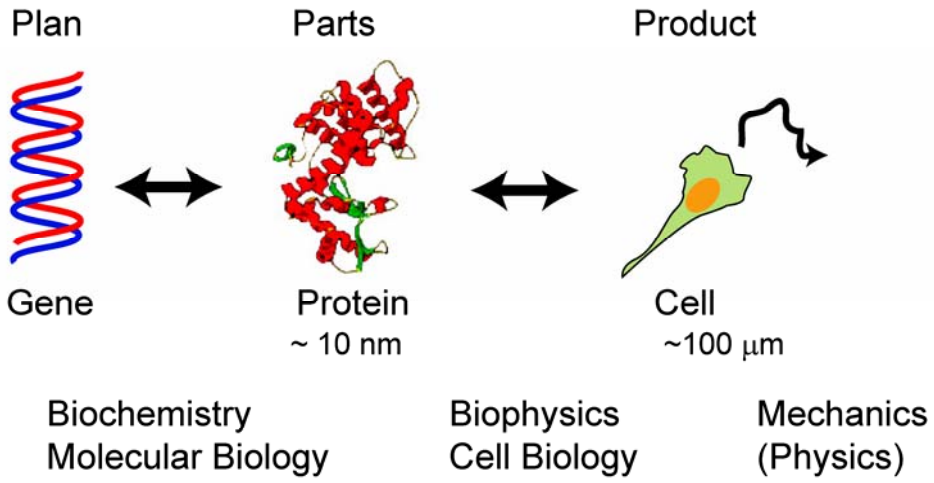

Figure 1.8 Various disciplines focused on different hierarchy of cell organization.

1.2.1 Cytoskeleton (actin filaments)

Ability of animal cells to carry out coordinated and directed migration depends mainly on a complex network of protein filaments that extends throughout cytoplasm. This network, called as the cytoskeleton, is composed of three types of protein filaments: actin filaments, microtubules, and intermediate filaments. Especially, actin filaments are believed to be playing a key role in cellular migration. A single actin filament (F-actin) is a two-stranded helical polymer of protein actin (G-actin), as shown in Figure 1.9. Even after polymerization into F-actin, the addition and dissociation of G-actin occur at either end of F-actin. Since rates of G-actin addition/dissociation differ at the ends, F-actin has polarity.

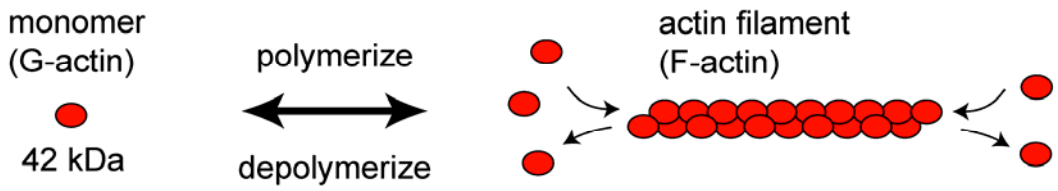

Figure 1.9 Actin is a globular protein with a molecular weight close to 42 kDa. Each globular actin (G-actin) polymerizes into actin filament (F-actin) due to self-binding sites on its surface.

F-actin in animal cells is highly distributed in the cortex, or just beneath the cell membrane. In this region, F-actin forms various types of array through an association with F-actin cross-linking proteins with different properties. Figure 1.10 shows major three types of cortical array of F-actin. In three-dimensional network of a cell cortex (A), F-actin cross-linked roughly at right angles develops as a loose and highly viscous gel. This gel-like structure is considered to give a cell mechanical strength. In contractile bundles (B), F-actin is arranged with opposite polarities and contains a motor protein myosin II (as explained in 2.4.1). This contractile structure is expected to be involved in drawing cell body forward and retraction of tail during cellular migration. In tight parallel bundles (D), F-actin is oriented with one direction. This structure is considered to be involved in extension at anterior portions of a cell.

When a fibroblast grows on a petri dish, most of its ventral surface is separated

from substratum; but at focal contact, cell membrane is locally attached to the dish. The focal contacts distributed discretely on substratum decide a cell shape. Attachment to and detachment from substratum are essential processes for cellular migration, as shown in Figure 1.7. At focal contacts, F-actin binds to substratum, being mediated by multiple attachment proteins, as shown in Figure 1.10(C) and Figure 1.11. Thus, F-actin is believed to be playing an important role in coordination of extension, retraction and attachment/detachment.

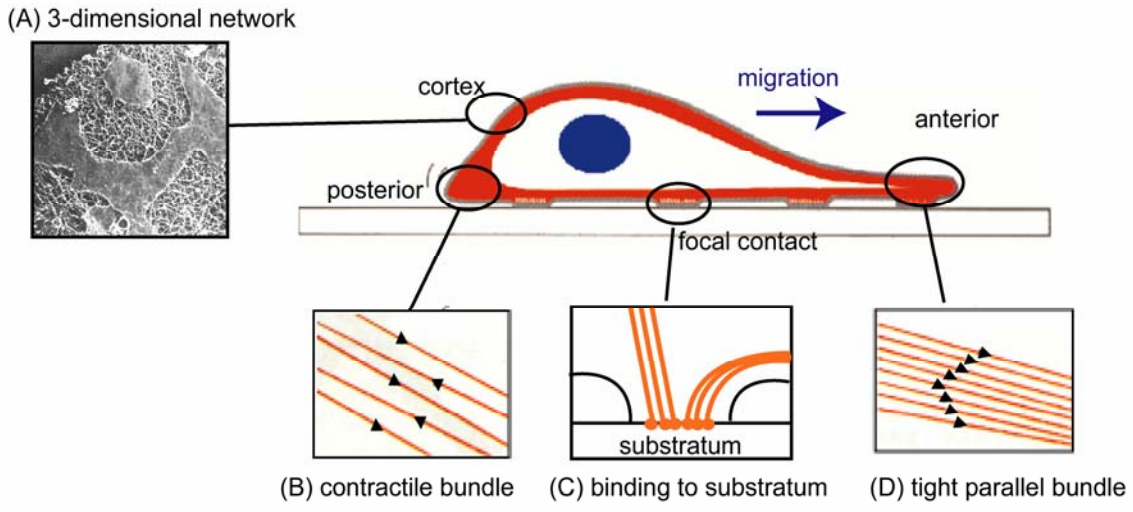

Figure 1.10 Three types of cortical arrays of F-actin (A, B, D). Arrow-heads indicate polarity of F-actin. F-actin also binds to substratum (C). (revised from [5, 6])

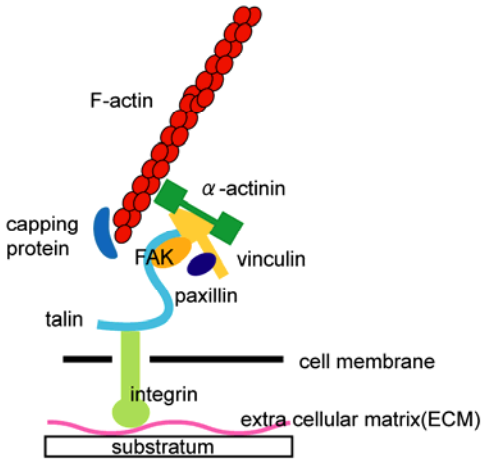

Figure 1.11 A possible arrangement of some of the attachment proteins that mediate the linkage between F-actin and substratum. F-actin binds to substratum indirectly through many proteins.

1.2.2 Approach from biomolecular functions and interactions

In a single cell, there coexist quiet different structures of F-actin networks bound by cross-linking proteins. Dynamic formation, disruption and rearrangement of these structures may be essential for cellular migration. Signaling proteins and signaling pathway regulating cellular migration have been intensively studied at the molecular level. Rho family of small GTPases including Rho, Rac and Cdc42 has been reported as a key regulator of cytoskeletal dynamics [7-10]. Figure 1.12 shows a signaling pathway for lamellipodium extension [11]. When a specific growth factor binds to a receptor, Rac and Cdc42 are activated. An integrin engagement with extracellular matrix (ECM) adsorbed to substratum also activates them. The activation of Rac and Cdc42 is postulated to act to F-actin accumulation in lamellipodia through several downstream targets. Here, active Rac and Cdc42 induce three types of rearrangement of F-actin as follows: (i) New F-actin polymerizes from the sides of existing filaments through a stimulation of Arp2/3 complex. (ii) F-actin is uncapped and generates extra sites for actin polymerization. (iii) F-actin is stabilized due to inhibition of cofilin-induced actin depolymerization. Since Rac and Cdc42 induce these rearrangements simultaneously, lamellipodium can be extended efficiently.

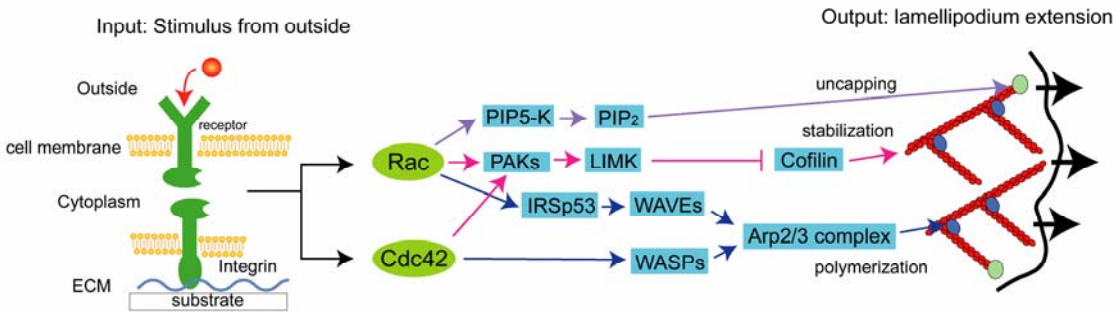

Figure 1.12 Rac/Cdc42-induced lamellipodium extension. Rac and Cdc42 can stimulates three types of rearrangements simultaneously.

Similarly, signaling pathways for retraction of tail and formation/dissociation of focal contact have been identified. However, if the subcellular processes such as lamellipodium extension, tail retraction and focal contact turnover occur independently, a cell cannot migrate in a direction. To achieve one step of cellular migration in a direction, four subcellular processes, shown in Figure 1.13, have to be coordinated temporally and spatially as follows: lamellipodium initially is extended (i), and attached to substratum (ii), and then, tail is detached off substratum (iii), and retracted (iv). The posterior portion is 100 μm distant from the anterior one in a cell. In contrast, signaling proteins are only several nm. So, signaling pathways dependent on interactions between the proteins are expected not to be able to cover a whole cell. Furthermore, one signaling protein often has ability to act to multiple targets inducing inverse subcellular processes such as extension and retraction. This, called as crosstalk, suggests that the signaling pathway is not a simple cascade, but a highly variable one that depends on its situation. Thus, a coordination mechanism for cellular migration is difficult to clarify at the molecular level.

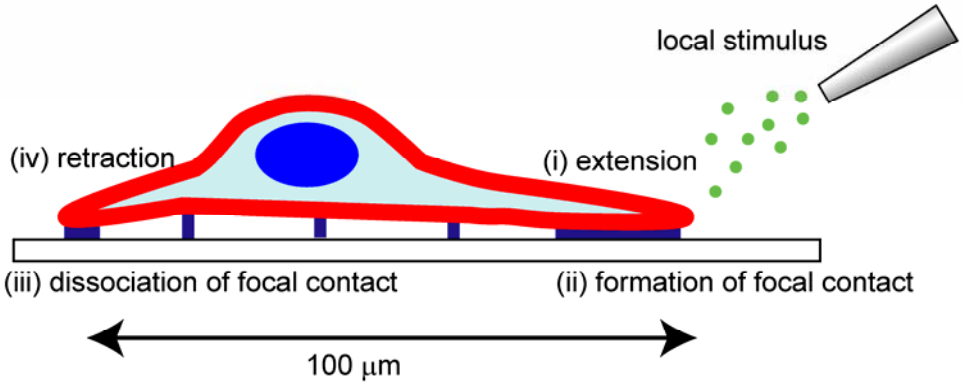

Figure 1.13 Cells have to coordinate at least four subcellular processes temporally and spatially in directional migration: (i) Lamellipodium extension and (ii) Formation of focal contact in the anterior portion, and (iii) Dissociation of focal contact and (iv) Tail retraction in the posterior portion.

1.2.3 Approach from mechanical properties of cells

Macroscopic studies focused on the mechanical properties at the cellular level are necessary to understand a mechanism of such integrated phenomena as a cell migration. To drag cell body forward in cellular migration, a cell must exert traction force on an external substratum. When cells are cultured on very thin sheets of flexible silicone rubber, the traction force that cells exert is made visible as elastic distortion and wrinkling of the substratum. Figure 1.14 shows this experiment reported by Harris *et al.* [12]. A cell indicated with *arrow* is highly polarized along the direction of migration and produces many pronounced wrinkles in the silicone rubber. Remarkably, the substratum wrinkles perpendicular to long axis of cell are seen throughout the region where the cell is adhering. This means that the cell exerts the traction force over the whole cell rather than generates it only on the local portion that would be retracted. In short, cell takes a step forward in manner of crawling motion like a worm does, as shown schematically in Figure 1.15. It is widely believed that this traction force originates in contractile structure of F-actin. Thus, the network of F-actin in the cell cortex, which includes contractile structure, possibly makes cells integrate mechanically.

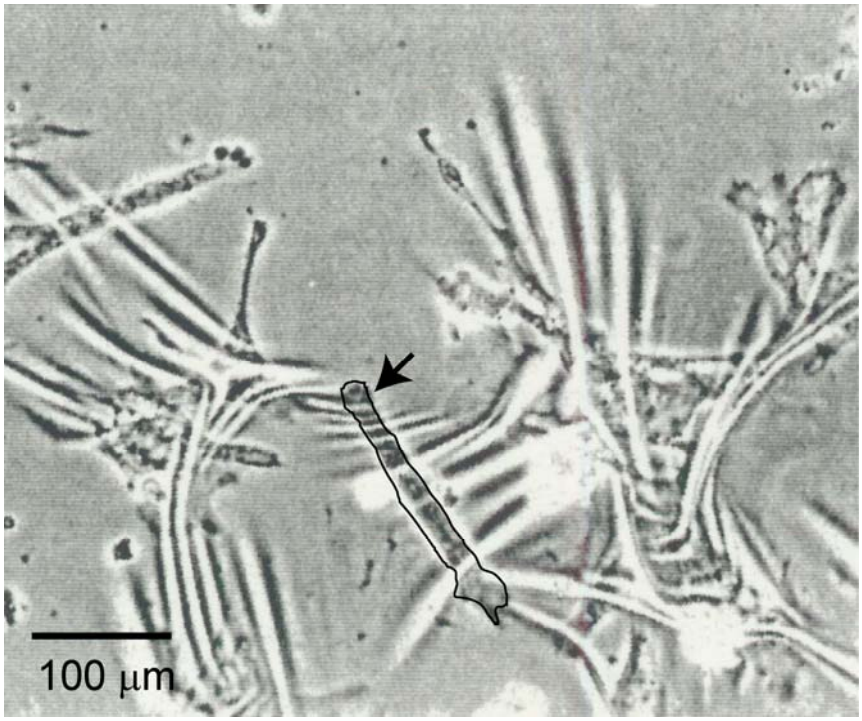

Figure 1.14 Wrinkles appearing on silicon rubber substratum on which cells attach. The wrinkles represent traction force that cells exert. [12]

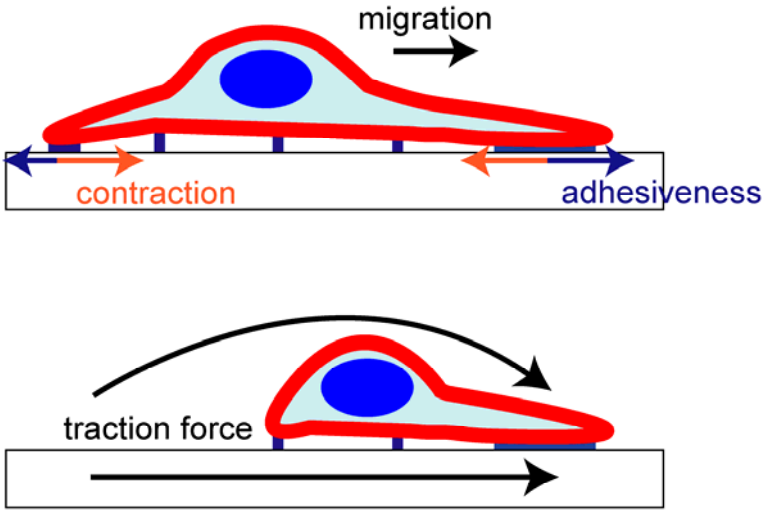

Figure 1.15 Schematic drawings of cell crawling. A cell takes a step forward like a worm. The cell would produce traction force in migration originating in its contractility by using anterior adhesion as a fulcrum.

A tensegrity model is proposed as a conceptual model of mechanical integration of a whole cell [13-16]. Figure 1.16 shows the tensegrity model constructed from six struts and elastic cord. Although the struts do not touch physically each other, they are pulled up and form an approximate sphere through interconnection with a continuous series of elastic cord (A). When this structure is anchored at multiple points to stiff substratum, it spontaneously flattens and spreads out without disrupting its structural integrity (B). This is due to variation of tension acting on each strut. When the anchors are removed, the structure spontaneously regains its original shape that is sphere. When the structure is anchored to a soft substratum, it spontaneously retracts, pulls its anchors together and hence, compresses the underlying substratum into folds (C). Living cells act in a nearly identical manner; they flatten and spread out when they adhere to petri dish (Figure 1.3), and they physically pull silicone rubber substratum into wrinkles (Figure 1.14). The tensegrity model focused on tension acting on network of F-actin provides a mechanical basis for coordination between part and whole.

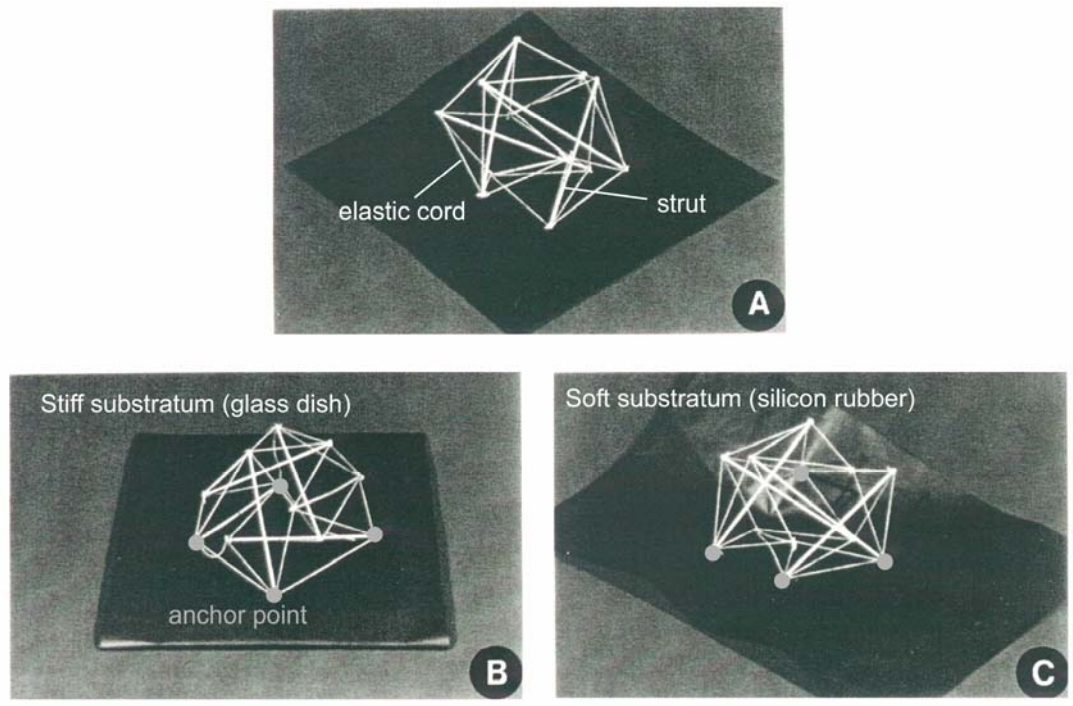

Figure 1.16 Tensegrity models constructed from six struts and elastic cord. The model appears round when unattached (A). The model spontaneously flattens when it is anchored to stiff substratum (B). In the case of soft substratum, the substratum is distorted with contraction of the model (C). This model can reproduce cell behavior. [13]

Recently mechanical properties of living cells have been focused on. A spatial distribution of quantitive traction force that a cell exerts has been obtained by using a flexible gel substratum [17]. Temporal variation of the traction force distribution according to cellular migration has been also reported [18, 19]. However, a relation between its traction force and mechanical properties of cellular cortex composed of F-actin has never been discussed. Mechanical properties of cellular cortex have been extensively studied using several techniques such as cell poking [20, 21], micropipette aspiration [22, 23], optical tweezers [24-26], and magnetic beads twisting [27-29]. Figure 1.17 shows schematic drawings of these techniques. In the cell poking method, relaxation decay of a cell membrane laterally indented by a glass stylus which is instantaneously withdrawn is measured. In the micropipette aspiration experiment, deformation of cell by suction pressure is measured. In the optical tweezers or magnetic beads twisting method, optical or magnetic beads attached to cellular surface are trapped with laser or magnetic field. When mechanical stress is applied to a cell through the beads, mechanical response of the cell is evaluated. Although mechanical properties of cellular cortex obtained by these methods are very significant, temporal and/or spatial resolution of these methods is not sufficient to discuss mechanical properties with respect to cellular migration.

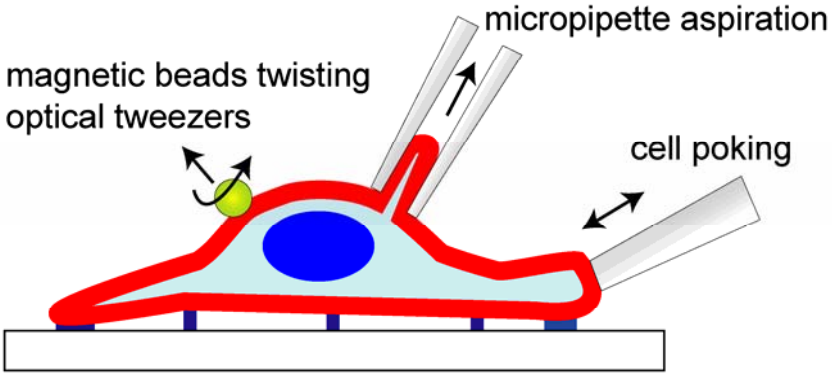

Figure 1.17 Schematic drawings of various methods for measuring mechanical properties of a living cell.

1.3 Scanning probe microscopy

An atomic force microscope (AFM), which is a kind of scanning probe microscope (SPM), is invented by Binnig and his collaborators in 1986 [30]. AFM has two remarkable advantages of not requiring conductivity of a sample and vacuum environment. Thus, AFM has rapidly developed as a powerful tool for imaging biological specimens at high resolution (in the nano-meter range) in their natural aqueous environment. In this section, operating principle of topographic imaging with AFM, and two methods for measuring viscoelastic properties of soft sample are described.

1.3.1 Topographic imaging

Figure 1.18 (A) shows schematics of AFM. Briefly, AFM images consist of a series of parallel line contours obtained by scanning sharp tip over surface of a sample. The tip is mounted at the end of cantilever, which has a small spring constant less than a hundred mN/m for measurements of a living cell. As the tip is scanned, an interaction force between the tip and the sample surface deflects the cantilever. In case of measurement at the molecular level, deflection of cantilever originates in atomic force between tip and sample. On the other hand, in case of measurement at the cellular level, the tip touches (more correctly indents) physically the sample rather than it senses atomic force. Then, in the present study, AFM is generally referred to as SPM. When the tip is scanned laterally over the sample surface, cantilever is deflected according to a change in height of the sample. The deflection of the cantilever is sensed by detecting angular deflection of a laser beam reflected off back of the cantilever, which is converted to electrical signals by photodetector. This signal is transmitted to scanner that the sample is placed on, and then an electronic feedback loop keeps the cantilever deflection constant by moving the sample up and down. The feedback allows the tip to trace over contours of the sample surface. An topographic image is obtained by plotting the vertical motion (z) of the scanner and hence the sample height (z) as a function of the sample lateral position (x,y). As the feedback always reacts with a little time delay, there will be small variations of deflection of the cantilever. A deflection image visualizing fine structure of sample surface is obtained by plotting this small deflection. This mode that can obtain topographic and deflection image simultaneously is usually referred to as contact mode or constant force mode.

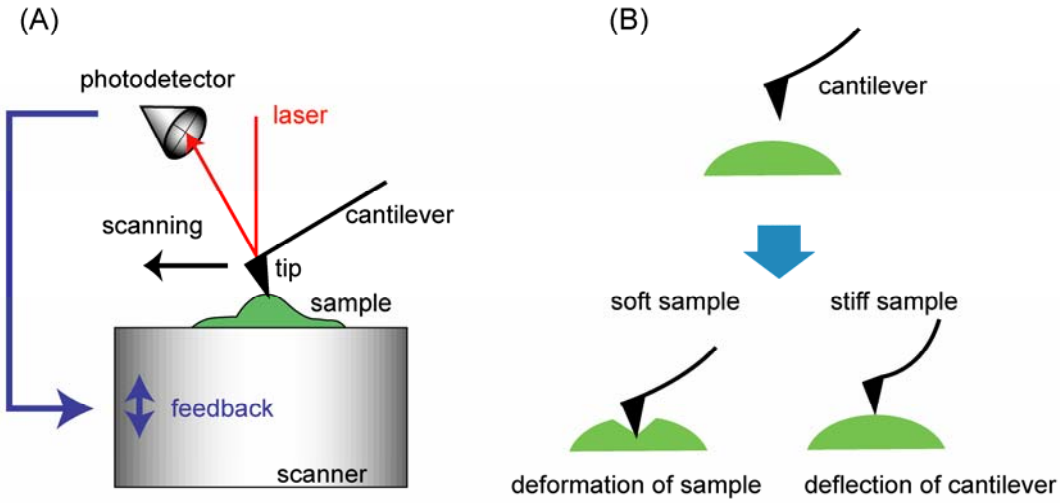

Figure 1.18 (A) Schematics of atomic force microscope (AFM). (B) A principle of measuring elasticity. When tip is indenting into sample, deflection of the cantilever is increasing in inverse proportion to deformation of sample. Thus, its deflection represents elasticity of sample.

1.3.2 Force mapping mode

As mentioned above, the tip is physically in contact with the sample in contact mode. This enables to obtain various mechanical properties of the sample surface such as adhesiveness and friction with SPM. Especially, recent studies have shown that viscoelastic properties of living cells can be detected with SPM. Figure 1.18(B) shows a principle of measuring elasticity of soft samples. Tip is indenting the sample vertically. In stiffer samples, cantilever deflects largely in proportion to decreasing distance to sample. In the softer samples, the cantilever little deflects due to deformation of sample. So, elasticity of sample can be evaluated quantitatively from relation between deflection of cantilever and indentation of sample, which is called a force curve. Details of this mode referred to as force mapping mode is described in 2.2.2. Figure 1.19(A) and (B) are topographic and elastic modulus images of a human platelet obtained by this mode, respectively [31]. The highest region in the topography represents a pseudonucleus. This region is softest (1.5 to 4 kPa), and stiffness of the outer region ranges from 10 kPa to 40 kPa. This study reveals that local stiffness is not homogeneous on cellular surface

but varies largely from point to point.

However, contributions of architectures of cytoskeleton to local stiffness and its distribution are still unclear. Moreover, it takes longer than 30 min to capture an elasticity image with 64×64 pixels. Such temporal resolution is too low for a detailed discussion on cellular migration.

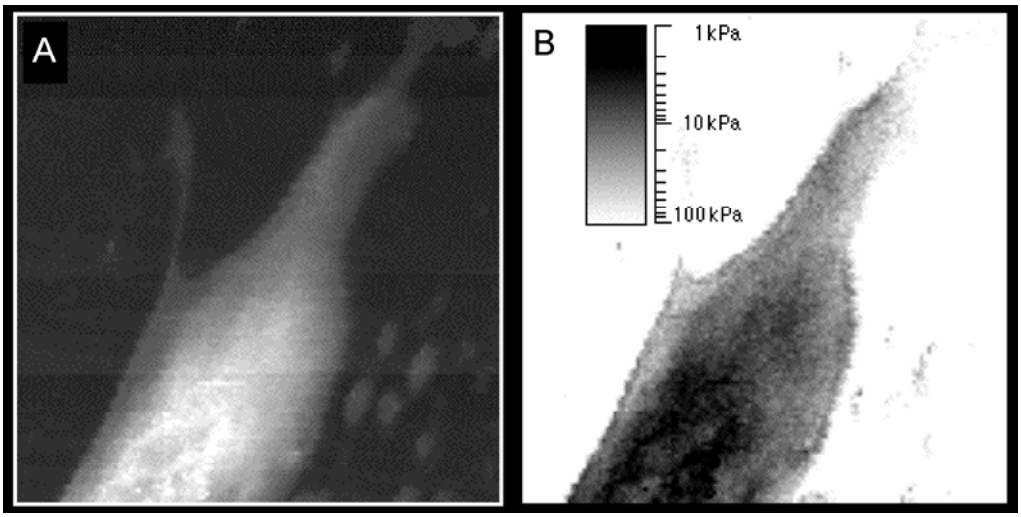

Figure 1.19 Topographic (A) and elastic modulus images (B) of a human platelet obtained by force mapping mode with SPM. The image size is 4.3 μm square consisting of 128×128 pixels. The range of gray scale in (A) is 2 μm. [31]

1.3.3 Force modulation mode

Force modulation mode is proposed in 1992 as another method for measuring viscoelastic properties with SPM [32, 33]. This mode can capture an elasticity image with higher spatial resolution in less than 10 min which is the same time scale as that for extending lamellipodia and retracting posterior portions producing cellular migration. Furthermore, it should be noted that this mode can evaluate not only elasticity but also viscosity of biological samples. In this mode, viscoelastic properties of a sample are estimated by applying sinusoidal stress to the sample instead of taking a force curve at each pixel. Figure 1.20 shows a principle of measuring viscoelasticity by this mode. An external vibration is applied to either a cantilever or a sample stage

during scanning in contact mode. This leads to a modulation of the force between tip and sample. The force modulation results in an indentation of the sample depending on its viscoelastic properties. As shown in Figure 1.18 (B), deflection of cantilever decreases in proportional to indentation of samples. In the previous works, qualitative elasticity and viscosity of the sample have been defined as an in-phase amplitude of cantilever deflection and a phase shift between excitation and response vibration, respectively.

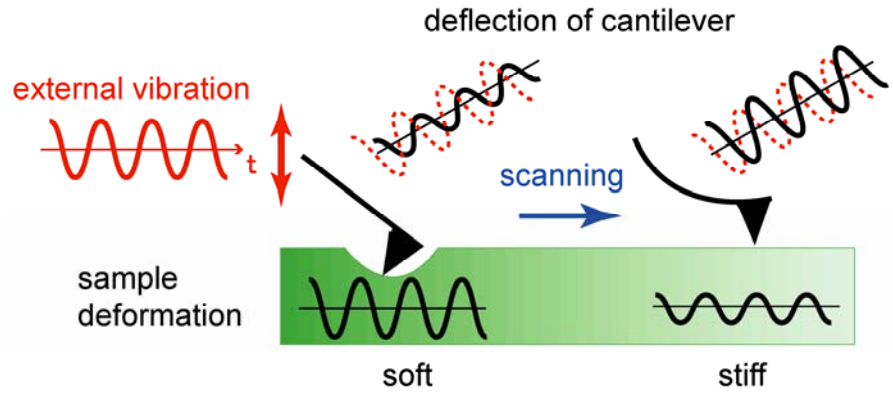

Figure 1.20 A principle of measuring viscoelasticity by force modulation mode. An external vibration applied to cantilever leads to a periodic indentation of samples. Sample elasticity and viscosity affect magnitude and velocity of cantilever deflection, respectively. Qualitative elasticity and viscosity of a sample can be evaluated from amplitude and phase shift of cantilever deflection, respectively.

Figure 1.21 shows topographic (A), amplitude (B) and phase shift (C) images measured by force modulation mode [33]. Modulation frequency applied to cantilever is 15.6 kHz. The sample is a polymeric diamino-diethylene glycol-pentacosadiynoic acid (DPDA) monolayer transferred by the use of LB-technology onto a silicon wafer. In each image, the brightness represents a higher relative value. The film shows feather-like distorted areas where it is torn into individual ribbons. In the amplitude image (B), the polymeric film appears darker than the substratum, which means that the film is softer than the substratum. In the phase shift image (C), the polymeric film appears brighter than the background. This means that the polymeric film is more viscous than the substratum. These results agree well with bulk viscoelastic properties of the film measured by another method.

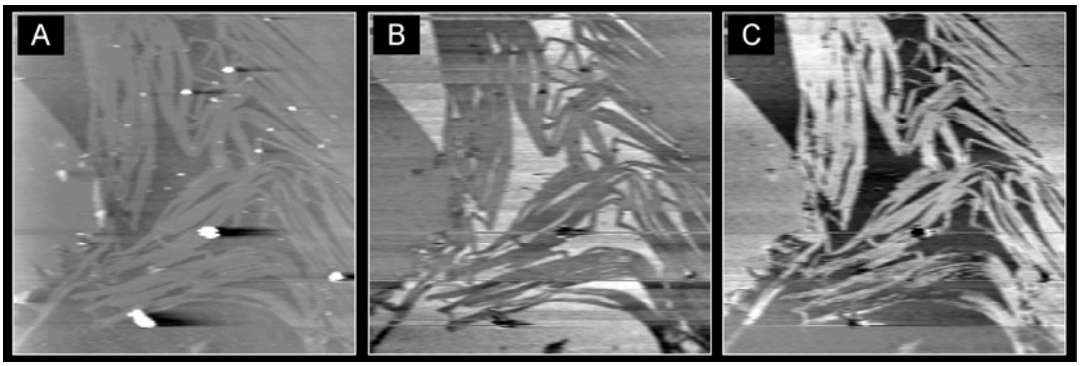

Figure 1.21 Topographic (A), amplitude (B) and phase shift images (C) of DPDA-monolayer obtained by force modulation mode. The image size is 4.3 μm. Image (B) and (C) represent elasticity and viscosity of sample, respectively. In each image, the brightness represents a higher relative value. [33]

However, in environment of liquid medium, cellular viscoelasticity obtained by force modulation mode is often incredible, even qualitatively. For example, cells sometimes look stiffer than a hard glass substratum in the elasticity images. This is mainly caused by influence of liquid viscosity and definition of viscoelasticity. A soft cantilever used for measuring cells has a spring constant of less than 20 mN/m. So, the influence of liquid viscosity on vibration of cantilever at high frequency above 10 kHz cannot be disregarded. Moreover, viscoelasticity of samples has to be defined as amplitude and phase shift of periodic sample deformation induced by external stress but not those of cantilever vibration. Thus, force modulation mode requires some improvements for measuring quantitative viscoelasticity of living cells in liquid cultured medium.

1.4 Purpose of the present study

Cellular migration plays a key role in biological and pathological phenomenon at tissue level. One step of cellular migration consists of two processes: extension of lamellipodium and retraction of tail. In adhesive animal cells, attachment and detachment from substratum is also important process for the migration. Such cellular migration composed of some processes has been studied intensively at molecular level. These studies focused on biochemical reactions can make a mechanism of each process clear. Cells have to coordinate each process temporally and spatially in a directional migration. The coordination mechanism is one of the most difficult subjects to explain from biomolecular viewpoint. Recently mechanical viewpoint begins to be focused on. From this viewpoint, some conceptual models of mechanical coordination at cellular level have been proposed. Although mechanical properties of living cells have been measured by various methods, temporal and/or spatial resolution of these methods has not been sufficient to clarify the coordination mechanism of cellular migration.

The purpose of the present study is to clarify experimentally how a single cell coordinates its extension and retraction in cellular migration at cellular level. We carried out a quantitative evaluation for stiffness on cellular surface with high temporal and spatial resolution. Force modulation mode with SPM is improved, taking into account influence of drag force of liquid. It is revealed that a spatial and temporal distribution of cellular stiffness originates in cytoskeletal structures, cellular migration and contractile force. A spatial arrangement of stress fibers and a temporal variation in focal contacts are observed in detail. We propose a tensional coordination in cellular migration. The mechanical coordination may give a major breakthrough in cancer biology and tissue engineering. In physics, the mechanical coordination can explain macroscopic dynamics in non-equilibrium systems.

Chapter 2 Experiments

2.1 Cell culture and sample preparation

Fibroblasts (NIH3T3) derived from mouse embryo are used for the present measurements, because of the following experimental requirements: (i) To bear against scanning with probe during SPM imaging, the cells have to adhere strongly to substratum. (ii) To study migration of a single cell, it is required that the cells have high motility and don't form cell-cell contacts. (iii) The cells with higher ability of the division can be cultured easily.

Fibroblasts have been purchased from RIKEN Cell Bank (Tsukuba, Japan) and are grown in plastic flasks filled with culture medium. The medium is composed of low glucose Dulbecco's modified Eagle's medium (DMEM) supplemented 10% fetal bovine serum (FBS) including some growth factor, which is essential for cell growth and proliferation (Gibco BRL, Basel, Switzerland). Suitable amount of antibiotics suppressing growth of fungi and bacteria is also added to the DMEM (Gibco BRL, Basel, Switzerland). The plastic flask is maintained at 37˚C and 5% CO_2 in a humidified incubator during cell culture. $NaHCO_3$ contained in DMEM acts as buffer keeping pH (7.3) under the condition of 5% CO_2. For experiments, confluent fibroblasts are tripsinized and are released from the flask. Then, its suspension are plated on a glass petri dish with a diameter of 30 mm and a height of 3 mm which have been precoated with fibronectin (Boehringer Mannheim, Mannheim, Germany). Fibronectin as extra cellular matrix (ECM) allows fibroblasts to adhere to glass dish. Fibroblasts plated on the dish are incubated again for at least one night to adhere thinly and firmly. To keep the pH constant at 7.3 during the SPM measurements performed in the environment of open air, preheated HEPES-buffer acting independently of CO_2 is substituted for the culture medium at least 1 hour before the measurement.

2.2 SPM imaging for living cells

2.2.1 Instruments

A commercial instrument composed of SPA400, which equipped with piezo scanner with a maximum *x-y* range of 100×100 μm and a *z* range of 10 μm, and SPI3800 control unit is used (Seiko Instruments Inc., Chiba, Japan). It is important to select a suitable spring constant of cantilevers less than 20 mN/m. When the spring constant is equivalent to that of cells, highest sensitivity for measuring the viscoelasticity is achieved. Three types of commercially available silicon-nitride cantilevers with a pyramidal tip that a typical radius of curvature is about 50 nm (ThermoMicroscopes, Sunnyvale, CA) are selected. The shape of the cantilevers are as follows: triangle with a effective length of 320 μm (type A), rectangle with length of 200 μm and width of 20 μm (type B), and triangle with a effective length of 220 μm (type C). According to calibration by thermal fluctuation method, spring constant of the cantilevers are 7.5 mN/m, 14 mN/m and 17 mN/m, respectively. During the measurement, a petri dish filled with HEPES-buffer has to be kept at the physiological temperature. The dish is placed on a metal plate kept at 33±0.5˚C by a temperature controller which consists of heater and thermocouple (see Figure 3.2). To prevent rapid evaporation of buffer, the temperature needed to be set about 5˚C lower than that on cell culture. Under these conditions, fibroblasts adhere thinly and firmly to the substratum over 3 hours even after SPM measurements. This verifies that physiological conditions are maintained during the present experiments and the scanning probe over cell surface does not induce any damage to fibroblasts.

2.2.2 Force Mapping Mode

Force Curve

Force mapping mode with SPM is generally used to measure Young's modulus of soft materials such as cell or gel. The principle is described schematically in Figure2.1. Cantilever is positioned above a sample surface (A), and then is gradually put close to the sample surface along the direction of *z* at constant speed. After the cantilever touches with it (B), the sample deforms and generates elastic force. For stiff samples such as glass (C), cantilever deflects in proportion to its *z* position. On the other hand,

for soft samples (D), relation between the deflection and the z position deviates from a linear one. Two deflection-versus-distance curves on stiff and soft sample are drawn in the figure. At each point on the curve, force induced by cantilever deflection, which obeys Hooke's law, balances with elastic force generated by indentation of sample. The curves indicate elastic response of samples. These are called force-versus-distance curve (force curve). To obtain spatial distribution of the Young's modulus over cell surfaces, force curves are taken repeatedly at each pixel point. In the present study, a single force curve is measured for 100 msec, and it takes about 40 min per one image consisting of 64×64 pixels.

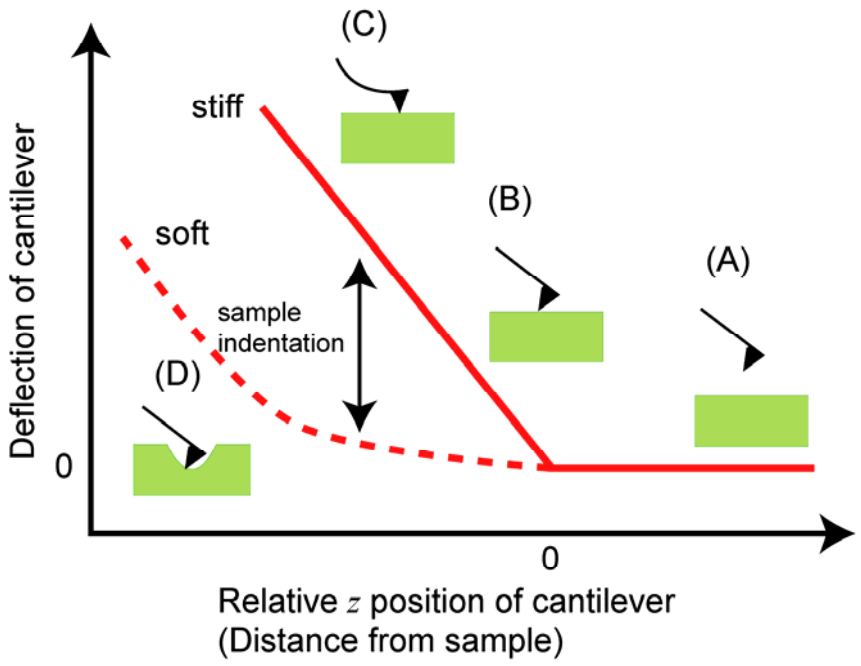

Figure 2.1 Typical force curves on a stiff (*solid line*) and a soft sample (*dashed line*). The insets (A-D) represent the state of cantilever and sample in each situation.

Sneddon model

To evaluate local Young's modulus of one point on a cell surface from the force curve, Sneddon model is adopted. The model is a theoretical model that elastic contact theory of Hertz is applied to contact of elastic plane and rigid body cone [34, 35]. According to the model, the relation between loading force F and indentation of samples δ is

described as follws:

$$F = \delta^2 \frac{2}{\pi} \frac{E}{1-\nu^2} \tan\alpha$$

where E, ν and α are Young's modulus, Poisson ratio of the sample and half-opening angle of the cone (refer to schematic shown in Figure 2.2), respectively. F is not linear function of δ, since increase in indentation δ induces expansion of contact area between the cone and the sample. This corresponds to the deviation from linear relationship shown in Figure 2.1(D).

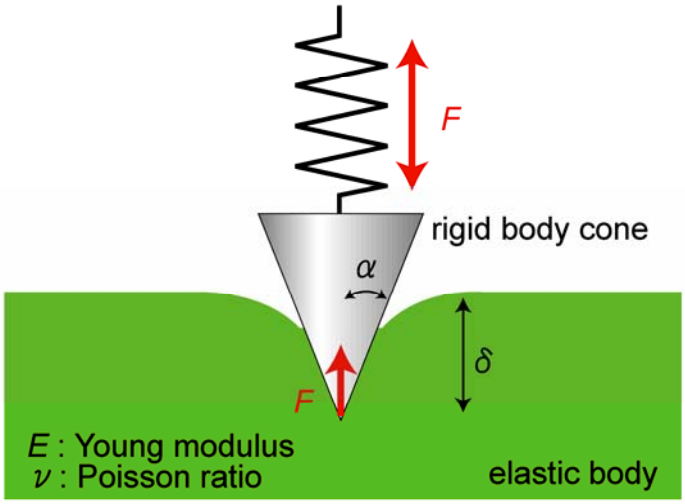

Figure 2.2 Force balance between rigid body cone and elastic plane. F is a loading force of the cone or an elastic force of the elastic body. α and δ are a half-opening angle of the cone and an indentation of the elastic body, respectively.

Fitting

Force curve is taken pressing cantilever onto a sample surface along the direction of z. Pressing by cantilever induces two mechanical deformations: Deflection of cantilever and indentation of sample. Taking this into account, the relation between relative z position of cantilever z and loading force F is given by the following equation:

$$z = \frac{F}{k} + \sqrt{\frac{\pi(1-\nu^2)F}{2E\tan\alpha}}$$

where k is a spring constant of cantilever. On the right-hand side, the first term expresses the cantilever deflection, which obeys Hooke's law. The second term originates in the sample indentation, which obeys Sneddon model. Fitting a force curve obtained by force mapping mode to this equation, local Young's modulus E can be evaluated as a fit parameter. Cellular Poisson ratio ν is assumed to be 0.5. The value of α is 35 deg, according to specification. Nonlinear least squares fitting (NLSF) is applied to a part of the force curve ranging from 0.1 nN to within 0.3 nN (or 0.5 nN) in the loading force. Figure 2.3 shows a typical force curve on a living fibroblast and its fitting curve. From fitting parameter, the value of E is evaluated as 6.97 kPa. The experimental force curve is reproduced well by the fitting curve. This means that Sneddon model sufficiently explains viscoelastic response of cells to pressing by cantilever.

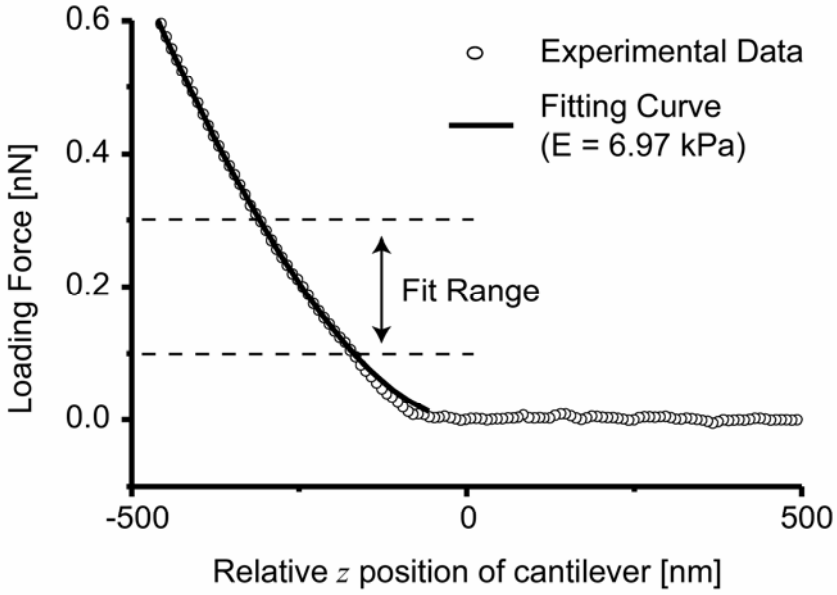

Figure 2.3 Typical force curve on a living cell (*open circle*). The force curve is good agreement with theoretical curve based on Sneddon model (*solid line*). Fitting range is from 0.1 nN to 0.3 nN.

2.3 Immunofluorescence imaging

2.3.1 Indirect immunofluorescent stain

In the present study, relation between cellular stiffness and higher order structure of cytoskeletal networks is revealed. To investigate a distribution of F-actin, myosin II and vinculin, each protein is labeled with antibodies by indirect immunofluorescent stain. The antibody secreted by lymphocyte binds itself selectively to particular protein called as antigen. Figure 2.4 shows schematic drawings of indirect immunofluorescent stain. Since a structure of the proteins is highly sensitive to environment, all proteins in a cell need to be cross-linked to fix before the stain. Primary antibody is bound to an antigen, and then, secondary antibody coupled to fluorescent molecule is bound to the primary antibody. In this method, because primary antibody is recognized by many fluorescent molecules of the secondary antibody, stained proteins can be easily detected with fluorescence microscopes.

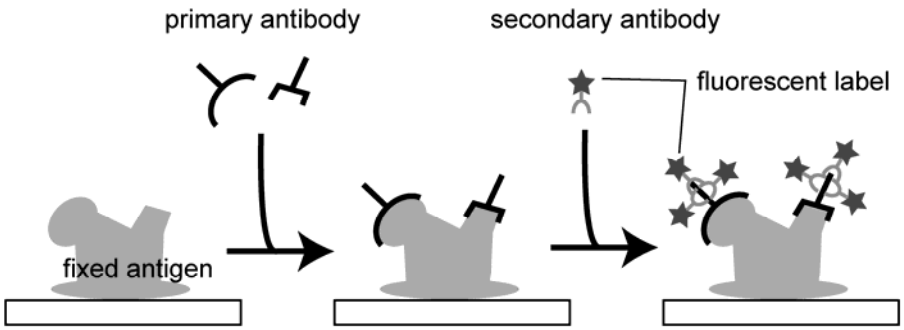

Figure 2.4 Schematic drawings of indirect immunofluorescent stain.

2.3.2 Protocol

Fibroblasts are washed once with PBS and are fixed with 4% formaldehyde/PBS for 10 min and then are washed again with PBS. After fixation, fibroblasts are permeabilized with 0.5% Triton X-100/PBS for 10 min and are washed twice with PBS, and then are incubated with PBS containing 0.5% bovine serum albumin (BSA) for 40 min. The permeabilized fibroblasts are incubated with primary antibodies/PBS containing 0.5% BSA for 1 h and are rinsed with PBS containing 0.5% BSA three times.

Then, the fibroblasts are incubated with secondary antibodies/PBS containing 0.5% BSA for 1 h and are rinsed three times again.

Myosin IIA is detected with 0.2% anti-human nonmuscle myosin IIA as primary antibody (gifted from Professor Masayuki Takahashi). Similarly, myosin IIB is detected with 0.2% anti-human nonmuscle myosin IIB as primary antibody (gifted from Professor Masayuki Takahashi). Both of myosin II recognized with primary antibody is stained with 0.4% Alexa Fluor 488 labeled anti-rabbit IgG (Molecular Probes, Inc., Eugene, OR) as secondary antibody. Vinculin is known as a major protein localizing at focal contacts. The vinculin is detected with 0.5% anti-human vinculin (Sigma-Aldrich, St. Louis, MO) as primary antibody, and 0.3% Cy3 labeled anti-mouse IgG (Jackson ImmunoResearch Lab. Inc., West Grove, PA) as secondary antibody. F-actin is labeled with 0.4 % FITC phalloidin (Sigma-Aldrich) or 1.0% Alexa Fluor 546 phalloidin (Molecular Probes, Inc., Eugene, OR).

2.3.3 Confocal Laser Scanning Microscopy

Fluorescence imaging is performed using a confocal laser scanning microscope (CLSM) equipped with 60× or 100× oil immersion objective (PCM2000, NIKON, Tokyo, Japan). Figure 2.5 shows optical components of CLSM schematically. A pinhole placed in front of laser source focuses excitation light at a single point in the specimen. A pinhole placed in front of detector eliminates fluorescence light except that emitted from the focal point. By scanning excitation light across the specimen, a sharp two-dimensional fluorescence image as shown in Figure 2.6 can be obtained. Furthermore, a three-dimensional impression can be constructed by stacking each sectional image obtained at various levels. Cytoskeletal structures on dorsal surface not including those on ventral surface and in cytoplasm can be visualized to compare with stiffness image measured with SPM. In the present experiment, Ar laser (λ = 488 nm) and He-Ne laser (λ = 543.5 nm) are used as excitation lights. Sectional fluorescence images are obtained every 0.3 μm in thickness.

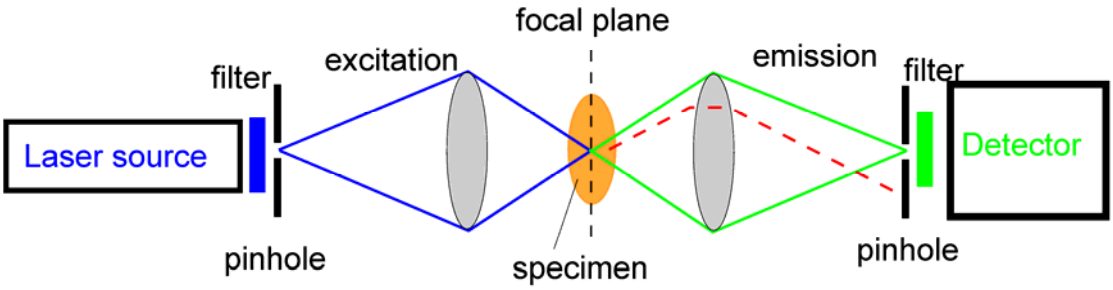

Figure 2.5 Simplified diagram of CLSM. An emitted fluorescent light (*solid line*) from in focus point in the specimen converges again at pinhole and reaches detector. By contrast, an emitted light (*dashed line*) from out-of-focus point is out of focus at pinhole and is largely excluded from detector.

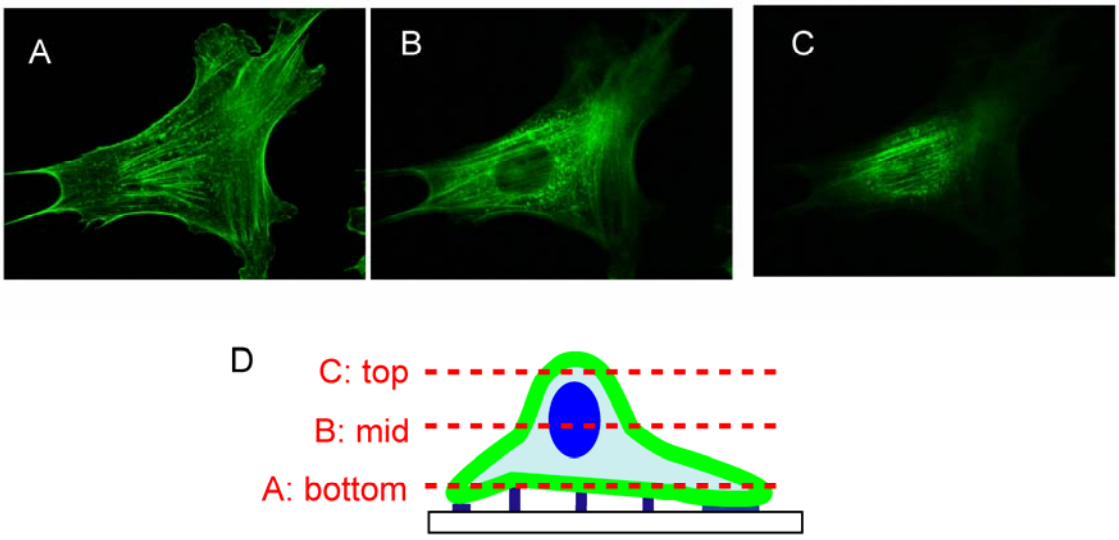

Figure 2.6 Two-dimensional fluorescent images obtained with CLSM (A-C). These images are taken at different height levels, schematically shown in (D), of an identical fibroblast. The fibroblast has been stained with a fluorescent probe for F-actin.

2.4 Regulating contractility with reagents

2.4.1 Myosin II

Myosin II as a kind of actin-binding proteins plays a key role in generating contractile force in a cell. Schematic diagrams of its conformation and function are illustrated in Figure 2.7. Myosin II possesses two head domains containing actin-biding site, and tail domain (A). Head domain moves toward the plus end of a F-actin by repeating hydrolysis of adenosine triphosphate (ATP). As shown in (B), the one cycle of movement is composed of four following steps: (i) A myosin head domain is bound to F-actin. (ii) ATP binds to the head domain, the domain is released from F-actin. (iii) When hydrolysis of ATP occurs, the domain is displaced along the F-actin by a distance of 5 nm. (iv) Release of inorganic phosphate causes the domain to bind again to F-actin. And this release triggers a force changing in shape. Adenosine diphosphate (ADP) is released from the head domain during change in shape. Finally, the domain regains its original conformation at the position 5 nm away from the initial position. Tail domain has an ability to form bipolar filament through the self-association. The bipolar filaments, due to its directional movement, can slide antiparallel F-actin over each other, thereby generating contractile force within F-actin network (C). The contractile force generated throughout a cell leads to intracellular contractility acting as the driving force in cellular migration. This is visualized in a silicon rubber substratum (Figure 1.14). In fibroblasts, temporary contractile bundle in which many F-actin and myosin II assemble, so-called stress fiber, is formed.

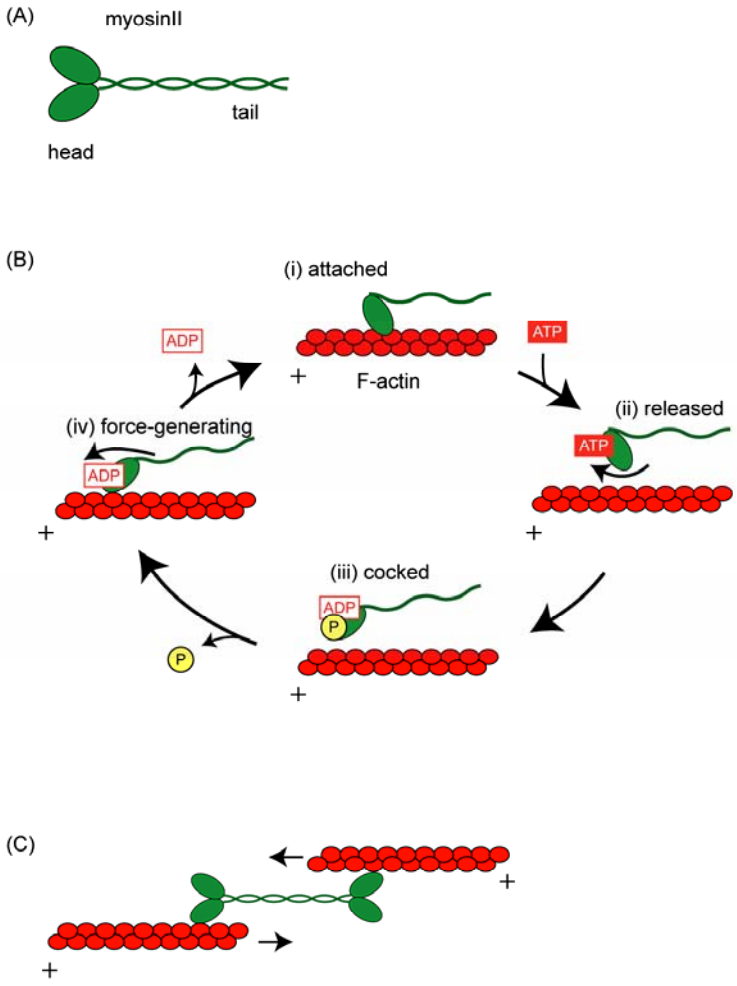

Figure 2.7 Structure and function of myosin II. (A) Schematic diagram of domain structure of myosin. (B) Four steps by which head domain of myosin II walks along an F-actin (C) A small antiparallel assembly of myosin II can generate local contractions in an F-actin bundle.

2.4.2 Biochemical reagents (LPA, Y-27632)

Phosphorylation of myosin regulatory light chain (RLC), which is a domain between head and tail, is essential to form stress fiber originating from interaction between myosin II and F-actin. It is known that the phosphorylation of RLC is regulated complementarily by two signaling pathways that involve (i) myosin light chain kinase (MLCK), which phosphorylates RLC; and (ii) myosin light chain phosphatase (MLCP),

which dephosphorylates RLC phosphorylated by MLCK [36-38]. Both activation of MLCK and inhibition of MLCP are possible to increase cellular contractility via actin-myosin II interaction. MLCK is activated by calmodulin bound to Ca^{2+}. On the other hand, MLCP is inhibited by Rho-associated kinase (ROK) without a change in Ca^{2+} concentration. The Ca^{2+}-independent pathway that regulates myosin II activity is shown in Figure 2.8. In the present study, fibroblasts are treated with two types of reagent that stimulate or inhibit ROK to regulate cellular contractility: Lysophosphatidic Acid (LPA) and Y-27632. LPA activates small GTPase RhoA via G-protein coupled receptor and guanine nucleotide exchange factors (GEFs). Then, ROK is activated by RhoA and inhibits phosphatase activity of MLCP subsequently. Consequently, LPA increases cellular contractility. Fibroblasts are stimulated by the addition of 5 μM LPA (Sigma-Aldrich, St. Louis, MO) to FBS free medium or HEPES-buffer. On the other hand, Y-27632 is known to be inhibitor of ROK. Treatment with Y-27632 reduces cellular contractility. Fibroblasts are treated by the addition of 20 μM Y-27632 (Calbiochem, San Diego, CA).

The petri dish is filled with DMEM without FBS, and then fibroblasts are incubated for one night before the experiments. The reason for using DMEM without FBS is that exception of soluble growth factor allows treatment with reagent to be effective in regulating actin-myosin II interaction. Under this condition, fibroblasts can adhere thinly to surface of glass dish due to precoated fibronectin.

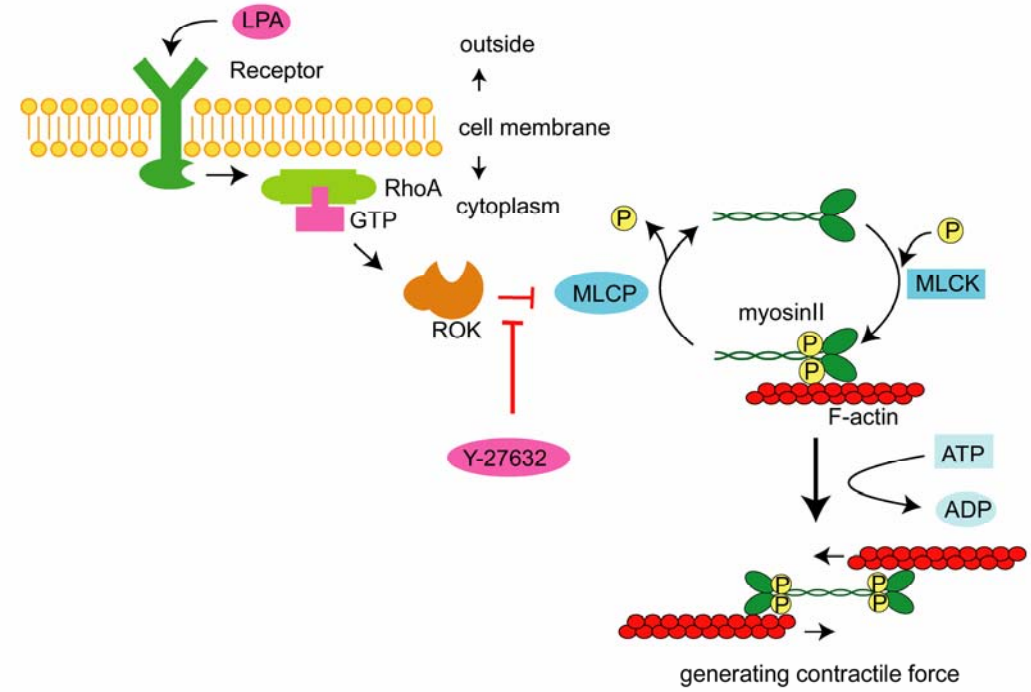

Figure 2.8 General model for regulation of contractile force via inhibition of MLCP through the RhoA/ROK pathway [36-38].

2.5 Interference reflection microscopy

Interference reflection microscope (IRM) invented in 1964 to measure the distances between cell and substratum [39-41]. IRM is known as a powerful tool for observing the state of cell-to-substratum adhesions in living cells. Briefly, IRM measures Fizeau fringes emerging due to the interference of wavefronts reflected at the phase boundaries created by thin layer of culture medium, which separates a cell and glass substratum. A principle of IRM is shown in Figure 2.9. The incident wavefront is split at each boundary in the series of phase boundaries as follows. When the incident monochromatic light has reached the glass substratum, it is partly reflected (reflection (i)), then the remainder of it travels to the glass/medium interface, where it is partly reflected (reflection (ii)). The light that has arrived at the medium/cell interface is split again into reflected (reflection (iii)) and transmitted wavefronts, and then the transmitted light is reflected again at the cell/medium interface (reflection (iv)). The interference of the reflections indicated with (ii) and (iii), results in Fizeau fringes. Because the phase of reflection (iii) is shifted $\pi/2$ when it is reflected at the medium/cell interface, an area where a cell is close to substratum is expressed as a dark area. Thus, the focal contacts appear as dark patches. In the present study, CLSM that has the emission filter removed is used for IRM observation. IRM can reveal dynamic properties of focal contact during cellular migration.

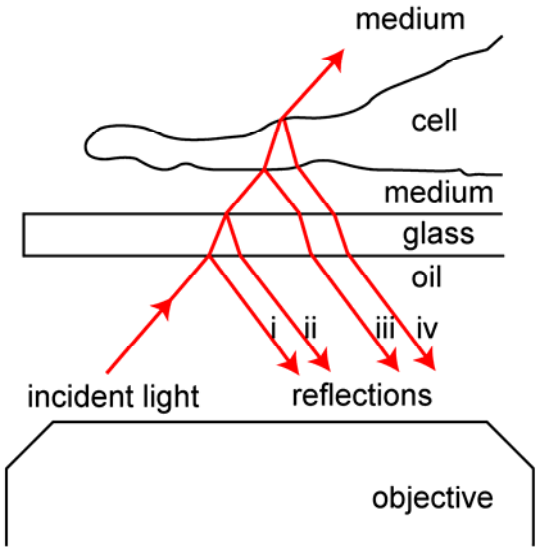

Figure 2.9 Ray diagram showing sequential spitting of an incident light at each boundary in the series of phase boundaries.

Chapter 3 Results and Discussion

3.1 Improvements of Force Modulation Mode

In this section, force modulation mode is improved and a quantitative method for evaluating cellular stiffness with high temporal and spatial resolution is established.

3.1.1 Modulation frequency

To examine effect of viscous drag on cantilever vibration, frequency dependence of its vibration is measured both in air and in liquid. Figure 3.1 shows the amplitude ratio when an external vibration ranging from 0.1 kHz to 10 kHz with amplitude of 10 nm is applied to an fixed end of a cantilever. Type B cantilever mentioned in 2.2.1 is used. In the inset, two conditions, that the tip of a cantilever is set on a glass substratum and is apart from it, are shown schematically. These conditions correspond to contact with infinite stiff and soft sample, respectively. The difference between two curves shows dynamic range of measurable stiffness. In air, two curves are parallel in the frequency range lower than 2 kHz. A peak appears at 5 kHz on both curves. It may be due to a mechanical resonance of the system, since the resonant frequency of the cantilever is listed as 12 kHz. In liquid, when the cantilever is set on the glass, amplitude of cantilever vibration is constant at lower frequencies than 3 kHz. In contrast, the cantilever, when it is apart from glass substratum, increases amplitude of its vibration gradually even at the low frequencies. This means that the cantilever vibration is affected strongly by viscous drag of the liquid. When the frequency exceeds 1 kHz, two curves cross each other. This leads reversed relation between the amplitude of cantilever vibration and the stiffness of sample. In this range of higher frequency, it is quite difficult to evaluate viscoelasticity of samples because viscous drag affects the cantilever vibration more than viscoelasticity of sample does. This suggests that frequency applied to cantilever in force modulation mode should be set lower than at least 1 kHz. When the frequency is selected lower, it takes longer time to capture a viscoelasticity image. Thus, the measuring frequency is chosen as 500 Hz. Even at this frequency, influence of the viscous drag of liquid is still comparable to that of the viscoelasticity of samples. This means that taking account of the viscous drag of liquid

medium is necessary for an accurate analysis of SPM cantilever vibration, described in 3.1.3.

A 128×64 pixels image can be obtained in only 6 min under this condition by this method. The spatial and temporal resolution of force modulation mode is 10 times higher than that of force mapping mode.

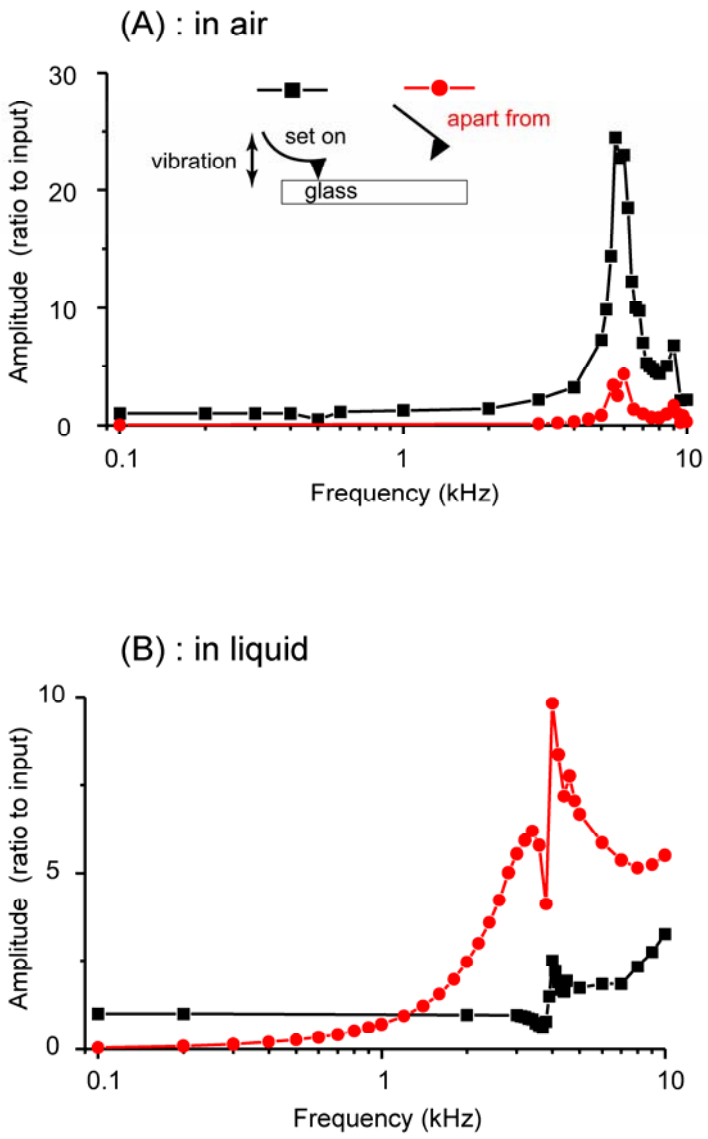

Figure 3.1 Frequency dependence of the amplitude of cantilever vibration in air (A) and in liquid medium (B). In each experiment, amplitude ratio to input vibration is taken under two different conditions where the cantilever is set on the glass substratum and is apart from it, as shown in the inset.

3.1.2 Set up of force modulation mode at low frequency

To measure topography and viscoelasticity of samples simultaneously at low frequency, SPM system is improved as follows.

When external stress is applied sinusoidally to samples, viscoelasticity can be estimated from an induced sinusoidal sample strain. Figure 3.2 shows a schematic of instrument used on the present measurements. On measuring viscoelasticity by force modulation mode, either a cantilever or a sample stage can be vibrated sinusoidally during scanning in contact mode. When the sample stage vibrates, sinusoidal voltage is applied to a scanner with a function generator (AFG310; SONY, Tokyo, Japan). In this mode, deflection signals of the cantilever consist of two components, which reflect topography (DC component) and viscoelasticity (AC component) of samples. These signals are detected by a position of laser on a sensitive photo detector. To evaluate viscoelasticity, the AC component of the deflection signal is extracted through a two-phase lock-in amplifier (Model 5210; PAR, Oak Ridge, TN), and then is visualized as amplitude and phase shift images.

On operating at frequency lower than several hundred Hz, the feedback circuit of SPM cancels the periodic signal to induce stress on samples. A band elimination filter (3624; NF, Yokohama, Japan) is put in the feedback circuit. The filter excludes AC component with frequency of the loading vibration from raw signals and sends only DC component to feedback circuit. As a result, the feedback system be only effective against topography of samples but ineffective against external oscillation. This is a major improvement on the instrument.

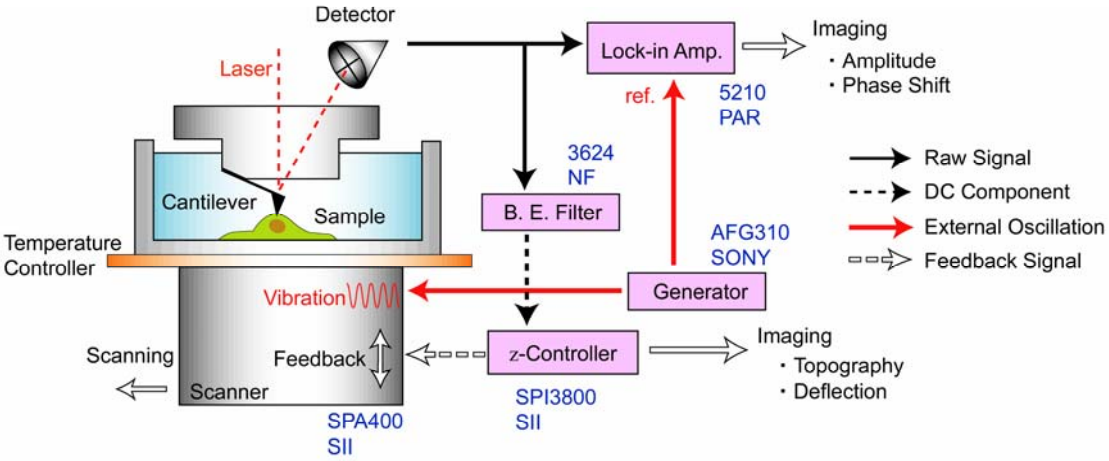

Figure 3.2 Schematic of SPM for force modulation mode operating at low frequency. The raw deflection signal is transmitted to both a lock-in amplifier and a band elimination filter (*black arrow*). This filter excludes only AC component with frequency of the loading vibration and transmits only its DC component to *z*-controller (*dashed black arrow*). The *z*-controller transmits feedback signals to a scanner by the DC component (*dashed white arrow*) and visualizes topography and deflection images. External oscillation from a function generator is sent to the scanner and the lock-in amplifier for vibration of sample stage and reference signal, respectively (*gray arrow*).

3.1.3 Analysis of cantilever vibration with viscous drag

It is not simple to estimate elasticity and viscosity of samples from amplitude and phase shift of the obtained signals, because the detected signals at the detector is not that of the sample strain but that of cantilever deflection. Furthermore, the quantitative evaluation requires to take into account the influence of viscous drag of liquid medium. In the present study, an analysis of SPM cantilever vibration including both effects of resistance force due to sample viscoelasticity and liquid drag against cantilever vibration is established. Overview of the analysis is given below. (Details of the analysis is described in Appendix.)

For a rectangle cantilever fixed at an end, shown in Figure 3.3, the one-dimensional differential equation on a vibration of cantilever in liquid is expressed as follows:

$$m^* \frac{\partial y^2(x,t)}{\partial t^2} + c^* \frac{\partial y(x,t)}{\partial t} + E_c I \frac{\partial y^4(x,t)}{\partial x^4} = p(x,t)$$

where *y(x,t)* and *p(x,t)* are deflection from a balanced position and loading force of the cantilever at position x ($0 \le x \le L$) and time t, respectively. L is the length of the cantilever. m^*, c^*, E_c and I are effective mass, effective damping coefficient, Young's modulus, and geometrical moment of inertia, respectively. The first term of the left-hand side expresses inertia. The second and third terms are viscous damping and elastic force of the cantilever, respectively.

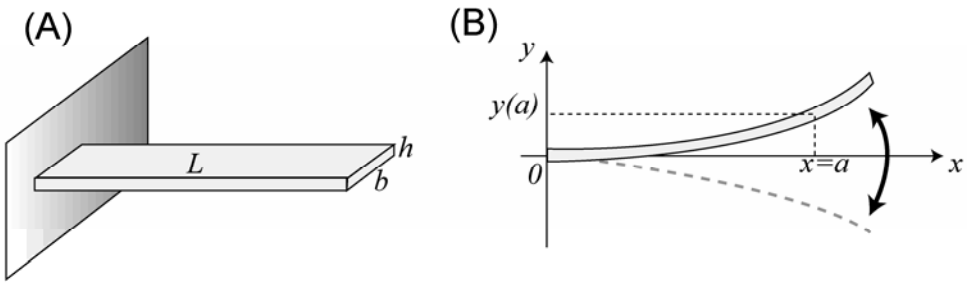

Figure 3.3 (A) Schematic diagram of cantilever. L, b and h are length, width and thickness of the cantilever, respectively. (B) One-dimensional deflection of the cantilever perpendicular to its length. *y(a)* is defined as deflection of the cantilever at position $x = a$.

Loading force *p(L)* at another end of the cantilever balances with elastic force originating in a viscoelastic response from sample. According to Figure 3.4, an indentation of sample is equivalent to $\phi - y$ when a vertical displacement ϕ of the sample causes a deflection y to the cantilever. The balance between the loading force and the viscoelastic response of samples is expressed as follows:

$$p(L,t) = -\left[K_s \{\phi(t) - y(L,t)\} + C_s \frac{\partial\{\phi(t) - y(L,t)\}}{\partial t} \right]$$

where, K_s [N/m] and C_s [N·s/m] are one-dimensional surface elasticity and viscosity of the sample, respectively. $\phi(t)$ is a vibration applied to the sample externally. The first and second terms of the right-hand side are elastic and viscous response, which are proportional to a magnitude and velocity of an indentation of the sample, respectively.

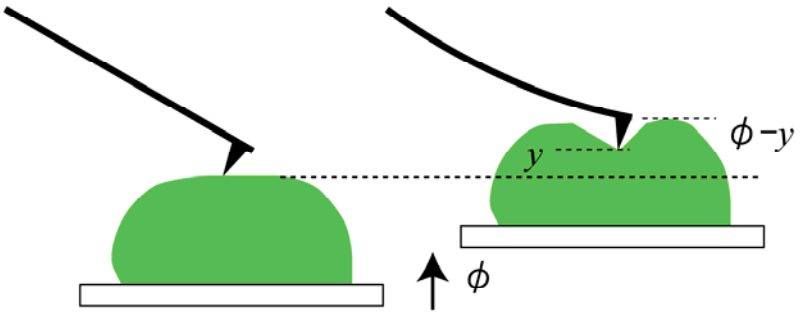

Figure 3.4 Schematic showing an indentation of sample induced by a vertical displacement of the sample or cantilever. When a vertical displacement ϕ of the sample (or cantilever) causes a deflection y to the cantilever, the indentation of sample is equivalent to $\phi - y$.

These equations allow to evaluate one-dimensional elasticity K_s and viscosity C_s from the detected amplitude and phase shift of the cantilever vibration signals. On Sneddon model, Young's modulus E [Pa] and coefficient of viscosity η [Pa·s] can be obtained from K_s and C_s by using equations described as follows:

$$E = \frac{\pi(1-\nu^2)}{8p_0 \tan\alpha} K_s^{\,2}, \qquad \eta = \frac{\pi(1-\nu^2)}{8p_0 \tan\alpha} K_s C_s$$

where p_0 is a pre-loading force on sample (= 0.4 nN). ν and α are Poisson ratio of sample (= 0.5) and half-opening angle of the cone (= 35 deg), respectively.

Generally, Young's modulus is defined as a value expressing elastic property of homogenous elastic or viscoelastic body. However, cells have heterogeneous structure. Moreover, a mechanical response from the cellular surface is expected to originate in many mechanical effects including structure of cell membrane and cytoskeleton, and osmotic pressure. In the present study, Young's modulus is regarded as an effective value of local stiffness rather than an elastic modulus.

3.1.4 Imaging

Figure 3.5 shows results for a living fibroblast measured by improved force modulation mode. These are topograpic (A), deflection (B), amplitude (C), phase shift

(D), stiffness (E) and viscosity images (F). Type B cantilever is used. The fibroblast extends very thinly on the substratum and highly polarizes on the image. Height of the fibroblast is about 2.5 μm. The highest region in the topography represents a cell nucleus (*dashed oval* in (A)). Many filaments beneath the surface running in parallel with the cell polarity can be seen clearly (*arrows* in (B)). In the amplitude (C) and the phase shift images (D), the values on the fibroblast indicate smaller amplitude and larger phase shift than those on the glass substratum, respectively. In the stiffness image (E), brighter areas represent stiffer ones. The values of Young's modulus are not uniform on the cellular surface but vary from a few kPa to 30 kPa depending on positions of the fibroblast. Although kind of cell is different, this is in good agreement with a quantitative result measured by force mapping mode (see Figure 1.19). In the viscosity image (F), brighter areas represent more viscous ones. The values of coefficient of viscosity are also not uniform on the cellular surface but vary from a few Pa·s to 30 Pa·s. The fibers seen in (B) are stiffer and more viscous than their surroundings (*arrows* in (E) and (F)). A sheet-like structure seen in a periphery region, which is lamellipodia, is very stiff and high viscosity (*arrow-head* in (A), (E) and (F)). This may be experimental artifact due to underlying glass substratum because its structure is only a few hundred nm in thickness, which is comparable to pre-indentation into cells in contact mode.

The values of coefficient of viscosity in nano scale have never been measured by other methods, and so validity of the viscosity image obtained by this method cannot be assessed. For this reason, only the topography and stiffness of cells are discussed in the following study.

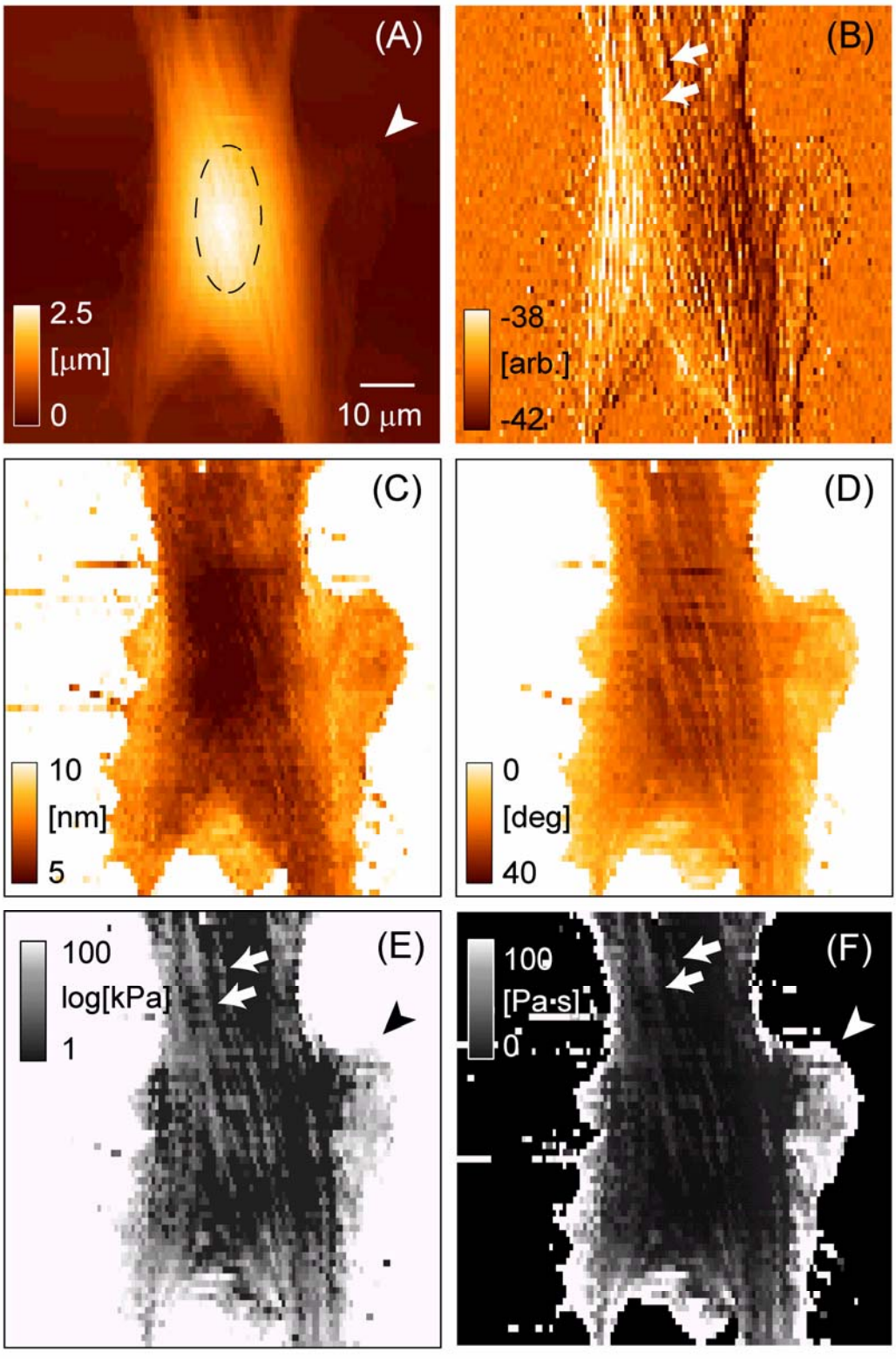

Figure 3.5 Topographic (A), deflection (B), amplitude (C), phase shift (D), stiffness (E) and viscosity images (F) of a living fibroblast measured by improved force modulation mode. The scale bar for stiffness in (E) is shown on a log scale. The bar in (A) is 10 μm.

3.1.5 Influence of surface roughness on stiffness

In force modulation mode, a morphology and viscoelasticity of samples are simultaneously taken as variations of cantilever deflection. The measurement is carried out during lateral scanning of a cantilever indented into sample surfaces. Both of the morphology and viscoelasticity may affect each other. To evaluate the influence of topographic roughness on stiffness image of samples, a line profile of the stiffness is compared with those of height and deflection. Figure 3.6 shows typical line profiles between *arrow-heads* in the inset. Several stiffer peaks appear on the line profile of stiffness (*circles*) corresponding with stiff fiber. Height profile has no sharp peak (*squares*). In the deflection profile (*triangles*), several peaks are observed at the same positions as the peaks in stiffness profile. When the peaks indicated with *arrows* are compared, it is found that the heights of stiff peaks have no correlation with those of deflection peaks. These results clearly verify that the surface roughness does not affect the stiffness data under the present condition (lateral scan speed = 64 pixels/s).

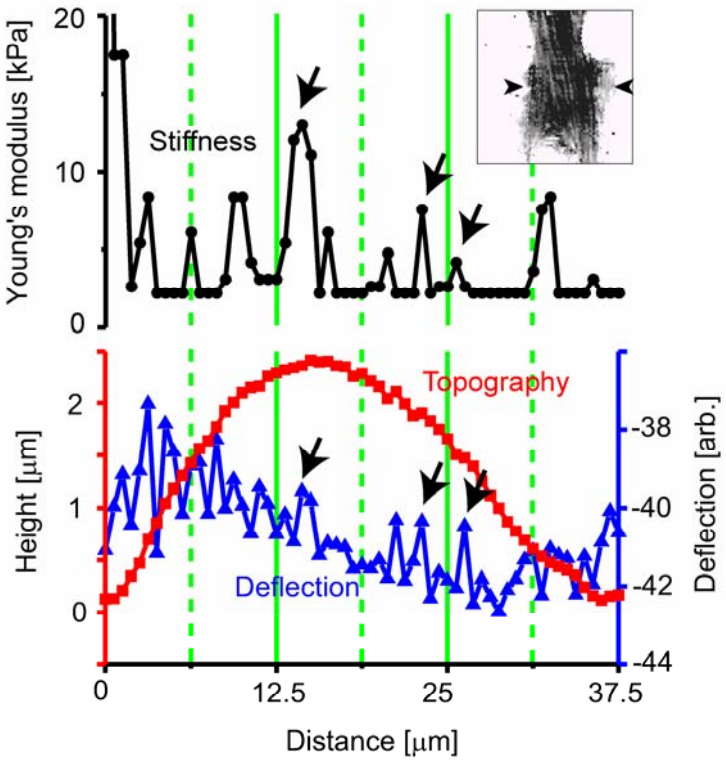

Figure 3.6 Line profiles (indicated with *arrow-heads* in inset) of stiffness, topographic and deflection images.

3.1.6 Verification of quantitative evaluation

Analysis of cantilever vibration, described in 3.1.3, allows to evaluate quantitative Young's modulus by force modulation mode. Young's modulus of fibroblasts evaluated by using this analysis corresponds roughly with that of a platelet measured by force mapping mode. This suggests that stiffness measured by improved force modulation mode is correct quantitatively. To verify the quantitative evaluation based on the analysis of cantilever vibration in further detail, Young's modulus of a same sample measured by the two methods should be compared. Figure 3.7 shows stiffness images of an identical fibroblast measured by force modulation mode (A) and force mapping mode (B), respectively. Type B cantilever is used in both measurements. In comparison between two images, stiff domains (denoted as *ovals*) in both of images, and soft domain (denoted as *dashed oval*) correspond in respect to its position and stiffness. Stiff fibers appearing in the (B) are not seen clearly in the (A). Stiffness at same positions in two images is plotted in (C). The fibroblast has almost changed neither its position nor shape during two measurements. Still, the surface structure is expected to drift within a few pixels. Then, the value is averaged over 3 pixels square. In the (C), it is revealed that two values measured by the different methods show a linear relation having its slope of almost 1. This proves stiffness measured by improved force modulation mode to be correct quantitatively.

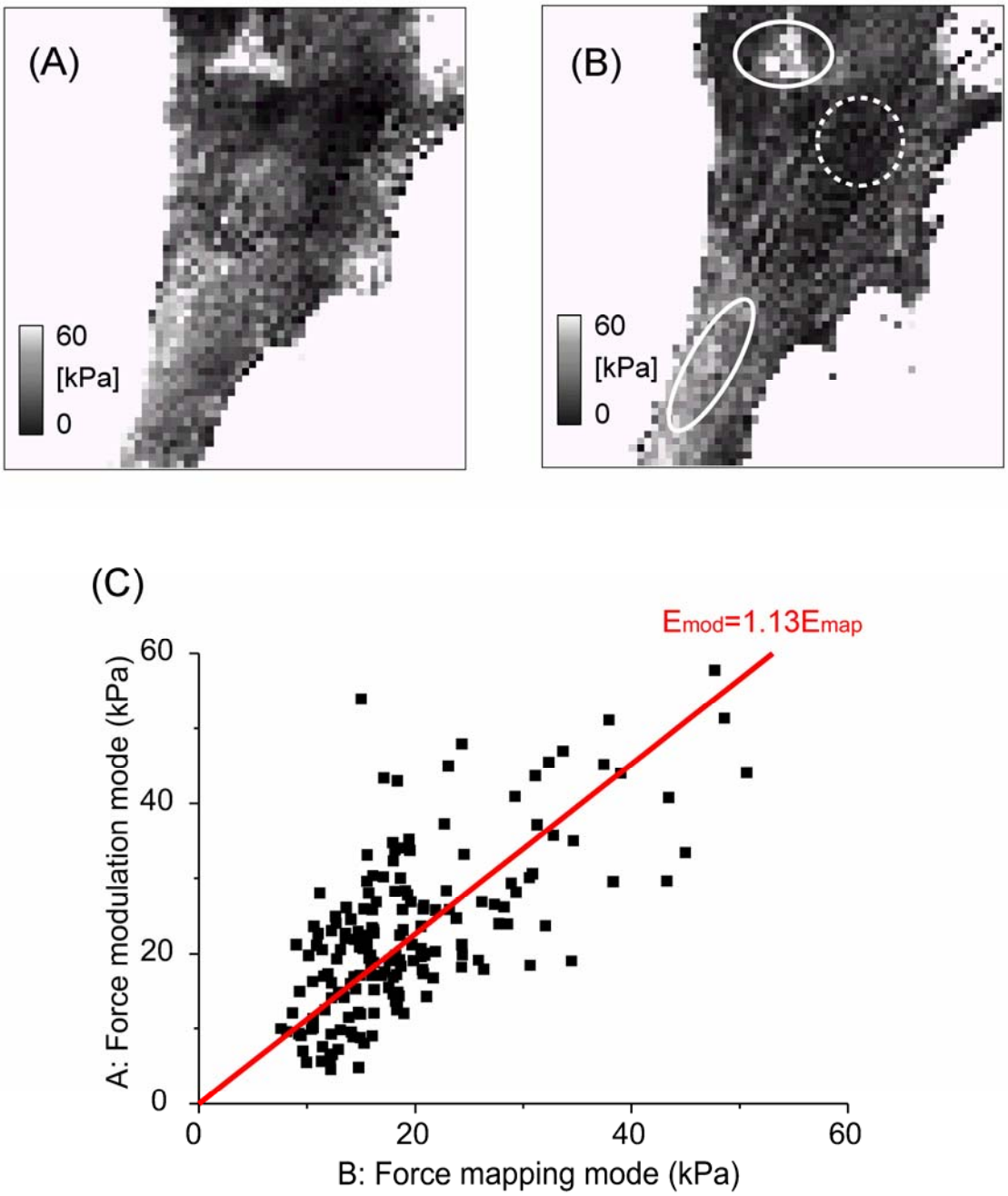

Figure 3.7 Two stiffness images of an identical fibroblast obtained by improved force modulation mode (A) and force mapping mode (B), respectively. Each image is 80 μm square consisting of 64×64 pixels. (C) A relation between stiffness at same positions in two images.

3.2 Origins of cellular stiffness

It is widely believed that cellular shape and stiffness result from cytoskeletal filaments, especially F-actin which is mainly distributed beneath cell membranes and is bound to substratum through focal contacts. In this section, relation between cellular stiffness and structures of F-actin is revealed directily. This suggests that F-actin gives cell mechanical stability as if acting such as a pillar and a roof.

To examine contribution of F-actin to cellular stiffness, immunofluorescence observations of an identical fibroblast are carried out just after SPM imaging. Figure 3.8 shows topographic (A) and stiffness images (B) measured by force modulation mode. The topographic image (A) is shaded using photo retouch software to render morphology of cellular surface more distinct. In this image, a few filamentous structures appear on the cell surface (*rectangle*). In the stiffness image (B), in addition to stiff filamentous structures (*rectangle*) corresponding with those in topographic image, two stiff domains also appear (*arrow-heads*). Distributions of F-actin on dorsal and ventral surface of the fibroblast are shown in Figure 3.8(C) and (D), respectively. Many filamentous structures are seen clearly in both images. Figure 3.8(E) shows a distribution of vinculin on the ventral surface, which represents positions of focal contacts. The filamentous structures composed of F-actin on dorsal surface terminate at focal contacts on periphery of the fibroblast (*arrows*) as if they cover the whole cell. On the other hand, the fibers on ventral surface are shorter than those on dorsal surface. They terminate at focal contacts within cell body (*oval*). Figure 3.8(F) shows these distributions schematically. By comparing images (C) and (D) with stiffness image (B), it is revealed that stiff filamentous structures and domains are accurately corresponding to the distribution of F-actin on dorsal surface (*rectangle* and *arrow-heads* in (C)) rather than that on ventral surface (D). The result suggests that cellular stiffness is mainly attributed to structures of F-actin which cover the whole cell surface and are bound to substratum at the cell periphery.

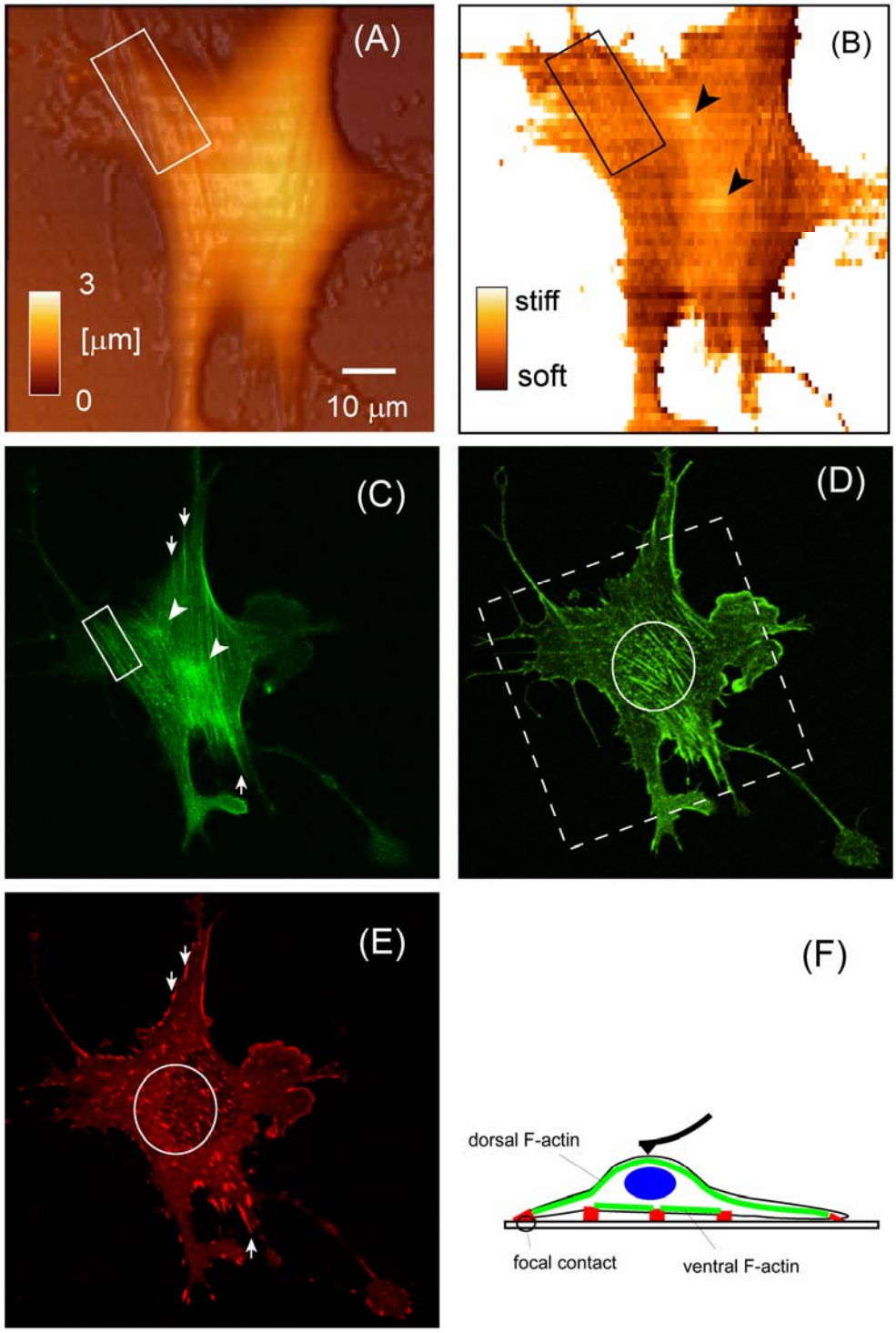

Figure 3.8 Topographic (A) and stiffness images (B) of a fibroblast measured by force modulation mode. Fluorescent images of F-actin on dorsal (C) and ventral surface (D), and vinculin on the ventral surface (E) of the identical fibroblast observed with CLSM. *Dashed square* in (D) represents corresponding area to SPM images. Schematic drawing (F) represents distributions of F-actin and vinculin in fibroblasts.

To verify such contribution of F-actin to cellular stiffness, a stiffness variation is measured when cytoskeletal filaments are selectively disrupted. Figure 3.9 shows stiffness variation in a fibroblast when F-actin is disrupted by treatment with Cytochalasin B. Figure 3.9(A) is stiffness image of a fibroblast measured by force mapping mode, and Figure 3.9(B) is that of the identical fibroblast at 30 minutes after the treatment with Cytochalasin B. The disruption of F-actin causes to reduce stiffness of the fibroblast drastically. Especially, an area above cell nucleus becomes about 10 times softer. On the other hand, disruption of microtubules by treatment with Nocodazole hardly affects celluar stiffness, as shown in Figure 3.10. The results reveal that cellular stiffness obtained with SPM originates mainly in F-actin cytoskeleton, but not in microtubules cytoskeleton, osmotic pressure, cell membrane, etc. The disruption of F-actin causes to shrink cellular shape, whereas the disruption of microtubules does not affect cellular shape. According to this, it is also revealed that F-actin cytoskeleton contributes to not only cellular stiffness but also cellular shape.

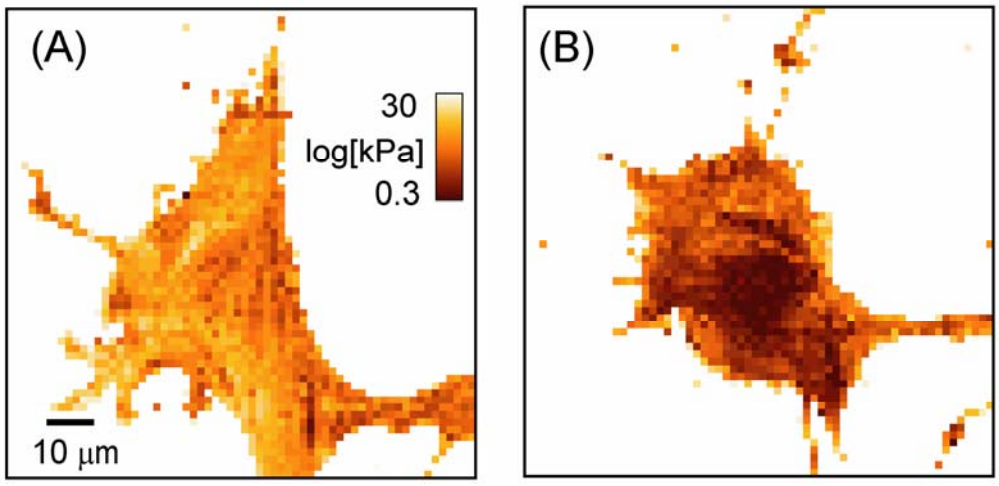

Figure 3.9 Stiffness images of a living fibroblast measured by force mapping mode before (A) and 30 min after disruption of F-actin (B). Each image is 80 μm square consisting of 64×64 pixels.

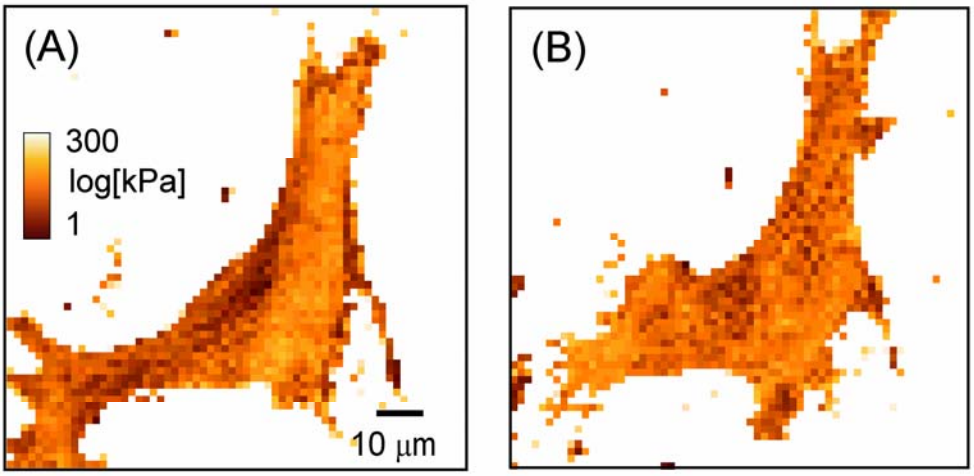

Figure 3.10 Stiffness images of a living fibroblast measured by force mapping mode before (A) and 30 min after disruption of microtubules (B). Each image is 80 μm square consisting of 64×64 pixels.

3.3 Temporal variation of cellular stiffness during migration

In this section, relation between the cellular stiffness and migration is revealed: When a cell is stationary at one position, stiffness distribution of cellular surface is quite stable. Once the cell begins to migrate, the stiffness in nuclear region decreases drastically.

To examine a variation of cellular stiffness during migration, a time-lapse series of stiffness images is obtained by force modulation mode. Sequential sets of topographic and stiffness images of a typical migrating cell are shown in Figure 3.11 and 3.12, respectively. The topographic and stiffness images are captured simultaneously every 10 minutes. Type C cantilever is used. SPM measurements are continued for about 90 minutes, which corresponds to an average time period of a one step on intermittent cell migration. In Figure 3.11, the fibroblast is changing its shape and is migrating downward in the image. The posterior portion of cell body (*oval* in (A)) is contracting, and a lamellipodia (*arrow* in (D)) is extending gradually during the measurement. Accompanying with the change in shape, the position of nucleus (marked by a *cross* in each image) is moving downward in the time course of images (A) through (F). In that of images (G) through (I), the position does not change, and several parallel fibers appear in lamellipodia (*dashed oval* in (H)).

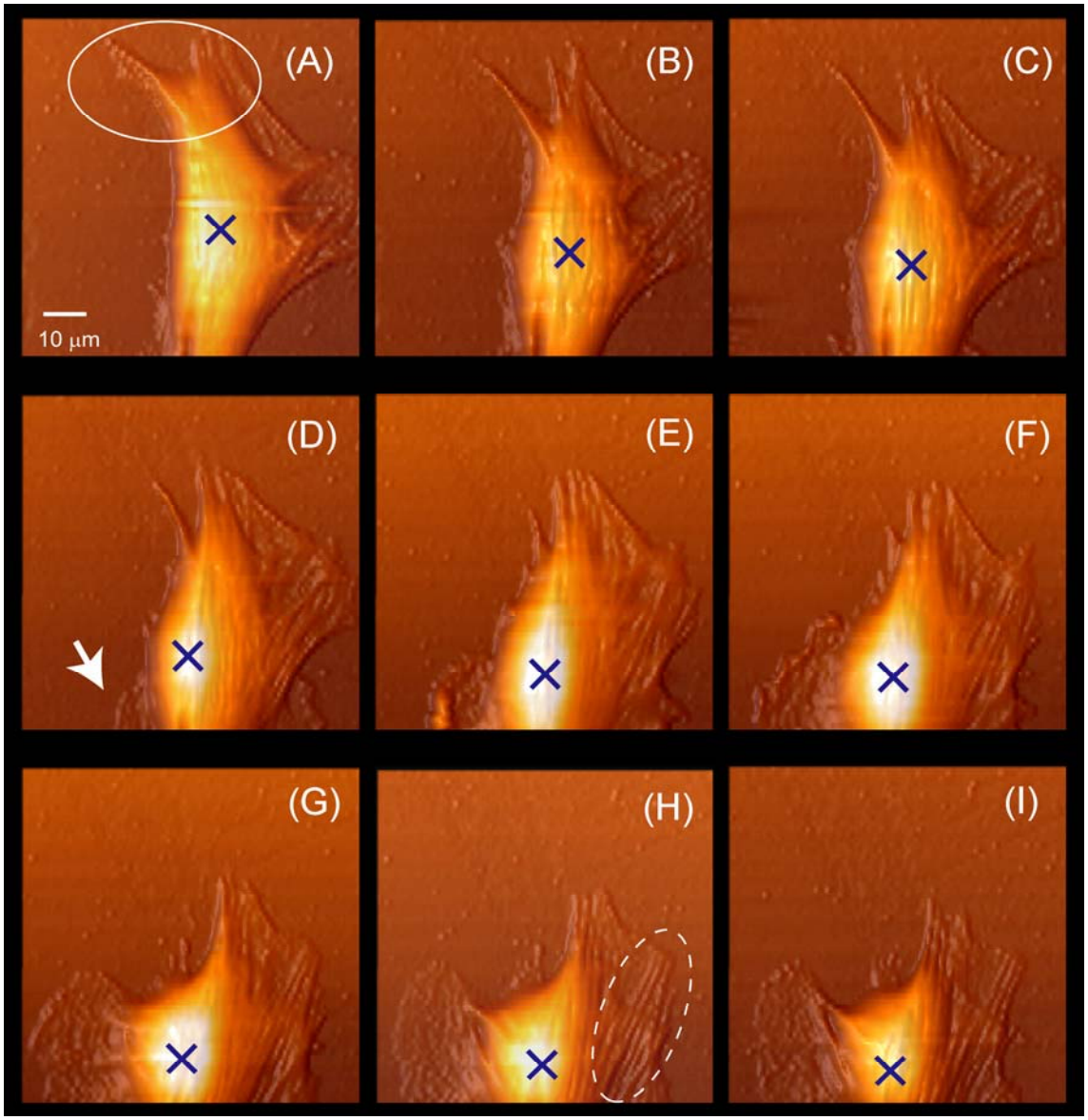

Figure 3.11 Time-lapse series of topographic images of a migrating fibroblast. All images are 80 μm square consisting of 128×64 pixels. These images are taken at 10 min intervals.

In Figure 3.12, it should be noted that the local stiffness distribution also changes drastically with the cellular migration. The area of nucleus within *oval* in the images (A) and (B) is harder than peripheral regions. Once the fibroblast begins to migrate, the nucleus region becomes drastically softer (*oval* in (F) and (G)). This result indicates that distribution of local stiffness correlates to cellular migration.

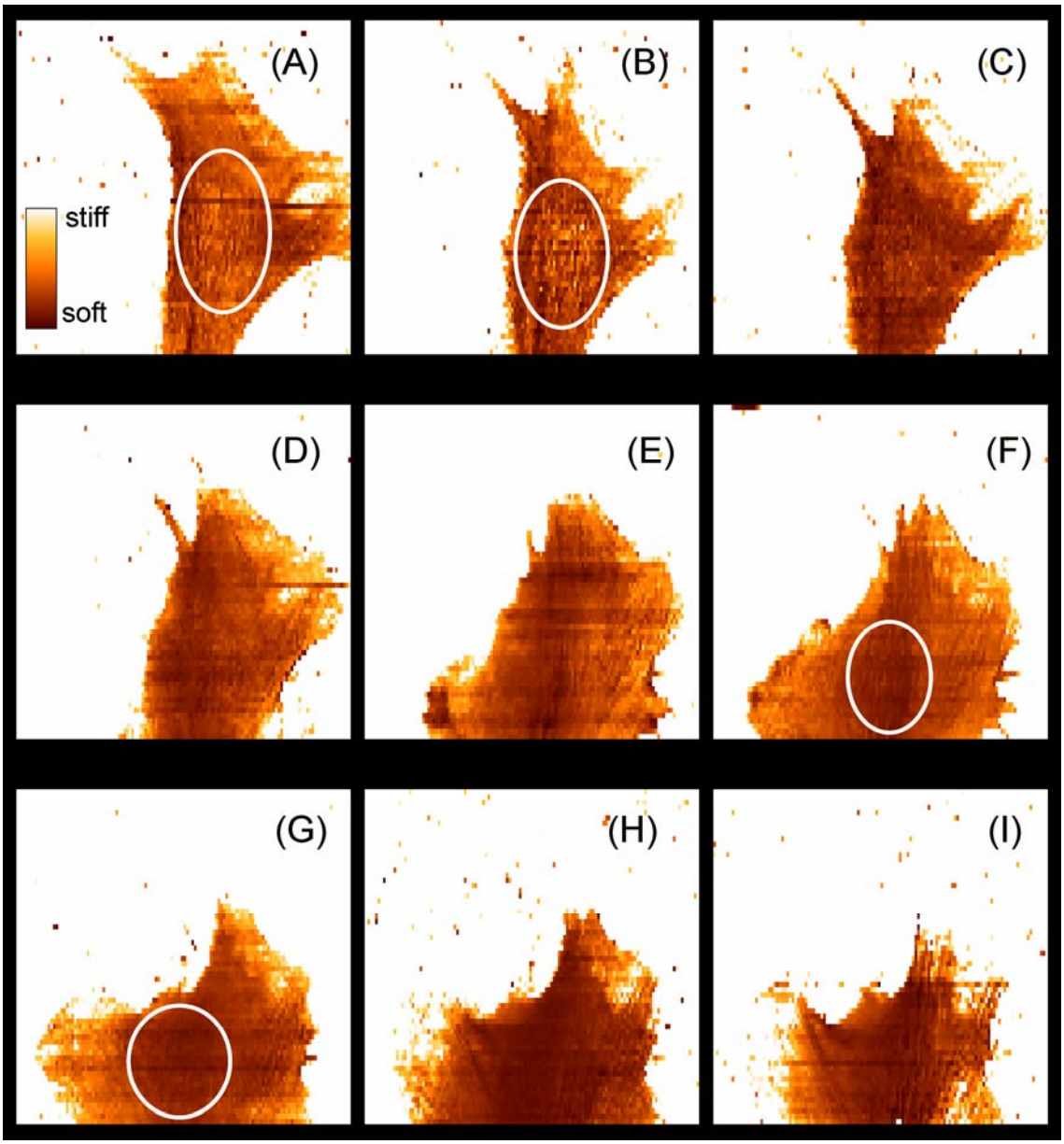

Figure 3.12 Time-lapse series of stiffness images of a migrating fibroblast. These images are obtained simultaneously with the topographic images shown in Figure 3.8. Each image is 80 μm square consisting of 128×64 pixels and is obtained by force modulation mode.

To confirm the relation between stiffness and migration, time dependence of local stiffness distribution of a fibroblast is also measured in the case that the fibroblast is staying at a position. Type C cantilever is used. Figure 3.13 shows sequential sets of topographic (A) and stiffness images (B) of a fibroblast over a period of 90 minutes. The

fibroblast does not change either its shape or its position during the measurement. In the stiffness images, stiffer stress fibers run across the entire cellular surface. In contrast with results on migrating fibroblasts, local stiffness distribution of the stationary fibroblast does not change temporally. This result indicates that stiffness of fibroblasts does not show any spontaneous periodic change, such as a cardiac cycle.

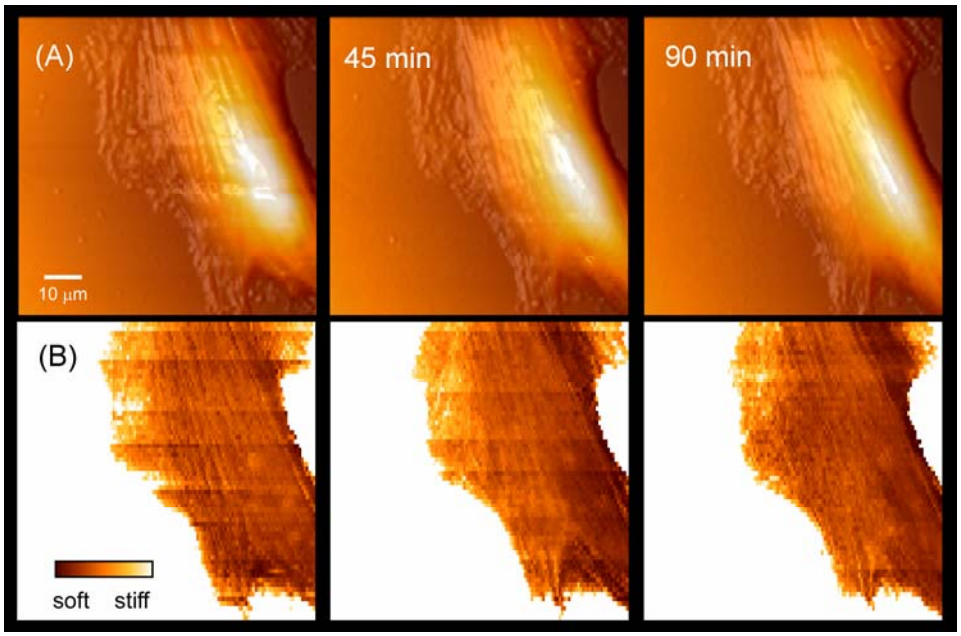

Figure 3.13 Time-lapse series of topographic (A) and stiffness images (B) of a stationary fibroblast. Each image is 80 μm square consisting of 128×64 pixels. Topographic and stiffness images measured simultaneously by force modulation mode are shown as a coupled image.

The displacement and the average values of the local stiffness at nuclear areas in both a migrating fibroblast (Figure 3.12) and a stationary fibroblast (Figure 3.13) are plotted as a function of time in Figure 3.14. In the migrating fibroblast (A), the stiffness at nuclear area drastically is decreasing when the fibroblast is migrating (till 50 min), and then the stiffness begins to increase when the fibroblast stops migrating. In contrast, the stiffness of the stationary fibroblast (B) is almost constant throughout this time period.

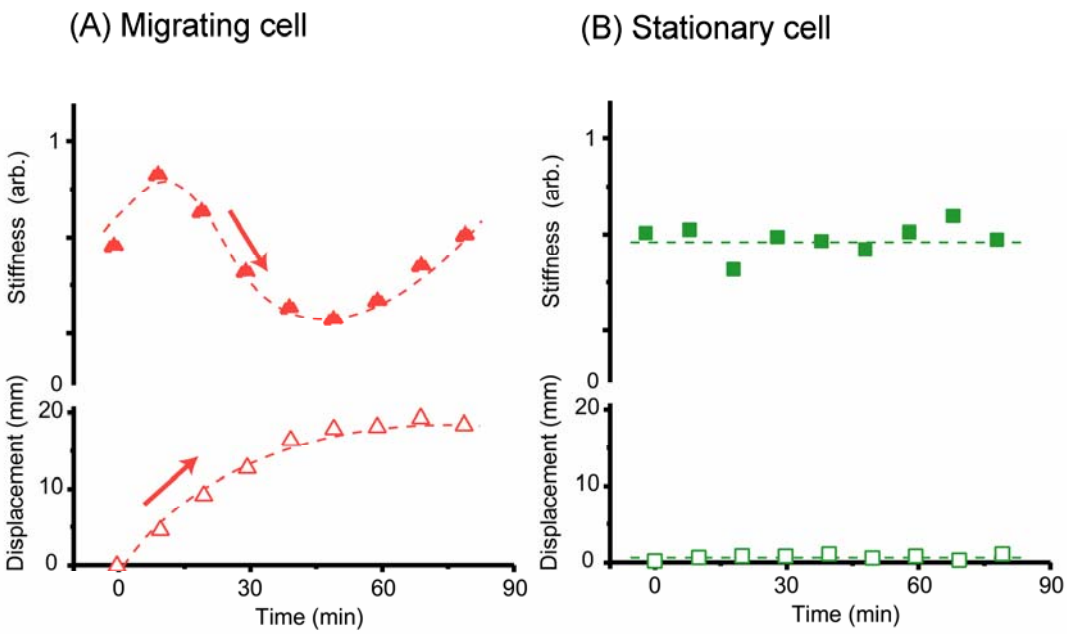

Figure 3.14 Time dependence of the stiffness at the nucleus region of the migrating (A) and the stationary cells (B). The migrating cell becomes softer (till 50 min), and then stiffer with time, whereas the stiffness of the stationary cell is almost constant.

3.4 Effect of cellular contractility on stiffness

In Section 3.2, it has been revealed that cellular stiffness mainly results from network structure composed of F-actin. As described in 2.4.1, F-actin forms contractile bundle through association with myosin II, called stress fiber. The contractile force generated by stress fibers can drag cell body forward during cellular migration. This suggests that a temporal variation of stiffness due to cellular migration revealed in Section 3.3 originates in a variation of this contractile force. In this section, it is revealed that cellular stiffness is attributed to cellular contractility.

3.4.1 Relation between stiffness distribution and contractile structure

Figure 3.15(A) and (B) are topographic and stiffness images measured by force mapping mode, respectively. Type A cantilever is used. In the stiffness image (B), many stiff fibers extending radially from a stiff domain (*arrow-head*) are seen clearly. The stiff domain is located in the neighborhood to nucleus, but surface area just above nucleus is softer than the surroundings. Figure 3.15(C) and (D) are distributions of F-actin and myosin II on dorsal surface, respectively. Although many fibers appear in both of images, these structures have a clear difference as follows: the fibers appearing in (C) are very sharp like a line, whereas those in (D) are seen like a dashed line composed of many dots arrayed on a line. Figure 3.15(E) shows the image that (C) and (D) are merged into. In this image, yellow area represents the region where F-actin and myosin are colocalized.

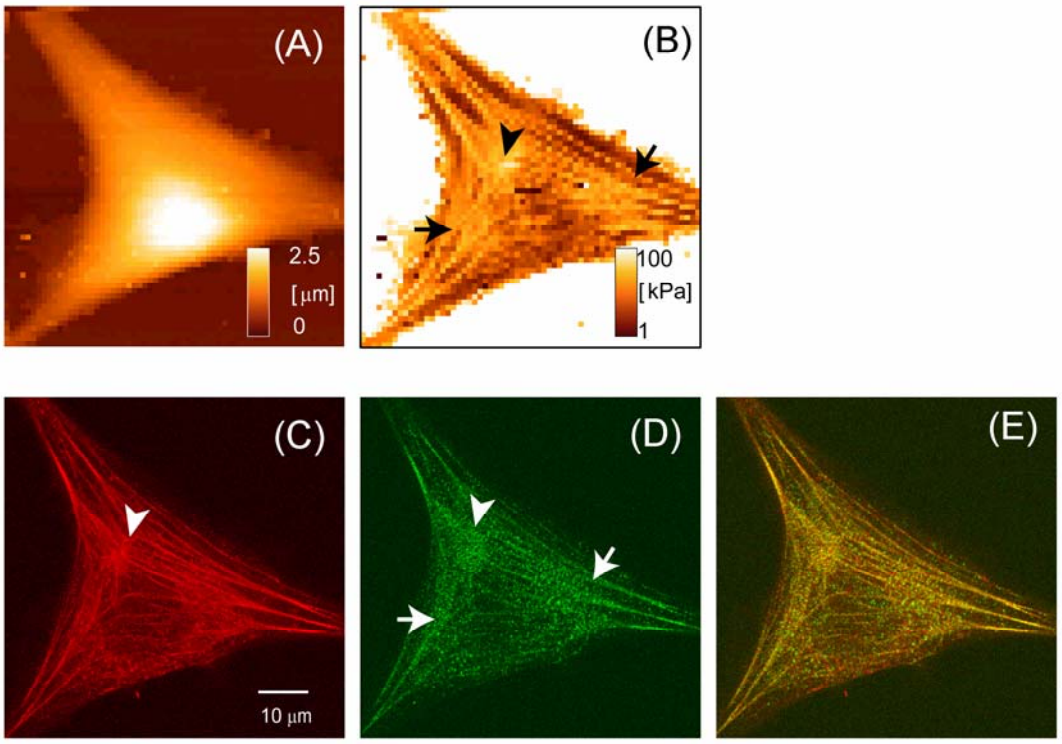

Figure 3.15 Topographic (A) and stiffness images (B) of a living fibroblast measured by force mapping mode. The distribution of F-actin (C) and myosin II (D) on dorsal surface of the identical cell obtained with CLSM. In merged image (E), red and green express F-actin (C) and myosin II (D), respectively.

Stiff fibers in (B) correspond well to the colocalized fibers in (E), namely stress fibers. Stiff domain (*arrow-head* in (B)) corresponds to where F-actin fibers converge (*arrow-head* in (C)). Although filamentous structure cannot be seen clearly in this domain (*arrow-head* in (D)), myosin II is highly concentrated. Two regions, which are similar in the distribution of myosin II, (*arrows* in (D)) also correspond to other stiff domains (*arrows* in (B)). This result suggests that cellular stiffness originates in not rigid but contractile framework composed of F-actin associated with myosin II.

3.4.2 Contractility effect of stress fibers on cellular stiffness

To examine a temporal relation with cellular stiffness and contractility, stiffness images are obtained when contractility is regulated by dosing of biochemical reagents. Figure 3.16 shows a variation in topographic and stiffness images of a fibroblast stimulated by LPA. These images are obtained by force mapping mode using type A cantilever. The stimulation by LPA increases cellular contractility. Figure (A) and (D) are topographic images before and 30 min after stimulation, respectively. Before stimulation, the fibroblast extends thinly on the substratum and highly polarizes with height of about 3.5 μm and lateral length of over 80 μm. A few lamellipodia can be seen. For 30 min after stimulation by LPA, the identical fibroblast extends some lamellipodia. Height of the fibroblast becomes about 0.5 μm lower. Figure (B) and (E) are stiffness images corresponding with the topographic images (A) and (D), respectively. Before stimulation, many stress fibers appear on cellular surface. Cellular surface above nucleus is softer than its surroundings. The stimulation by LPA raises stiffness of not only stress fibers (*arrow-heads*) but also whole of the cell. However, cellular surface above nucleus is still softer than its surroundings. Figure (C) and (F) show the distribution of stiff structures extracted from images (B) and (E). The stimulation by LPA makes new stiff domains appear on cellular surface near the nucleus.

The drastic increase of the cellular stiffness due to stimulation by LPA has not always been observed in all experiments. In the eight experiments, 50% fibroblasts became stiffer but the others did not vary its stiffness. Although further experiments are still needed, this may suggest that whether cells respond or not is dependent on cellular conditions even if they are stimulated by same reagent. Once cells respond to stimulation by LPA, they are expected to show drastic increase of the cellular stiffness, shown in Figure 3.16, without exception. This is partly supported by the result that stimulation by LPA has never reduced cellular stiffness.

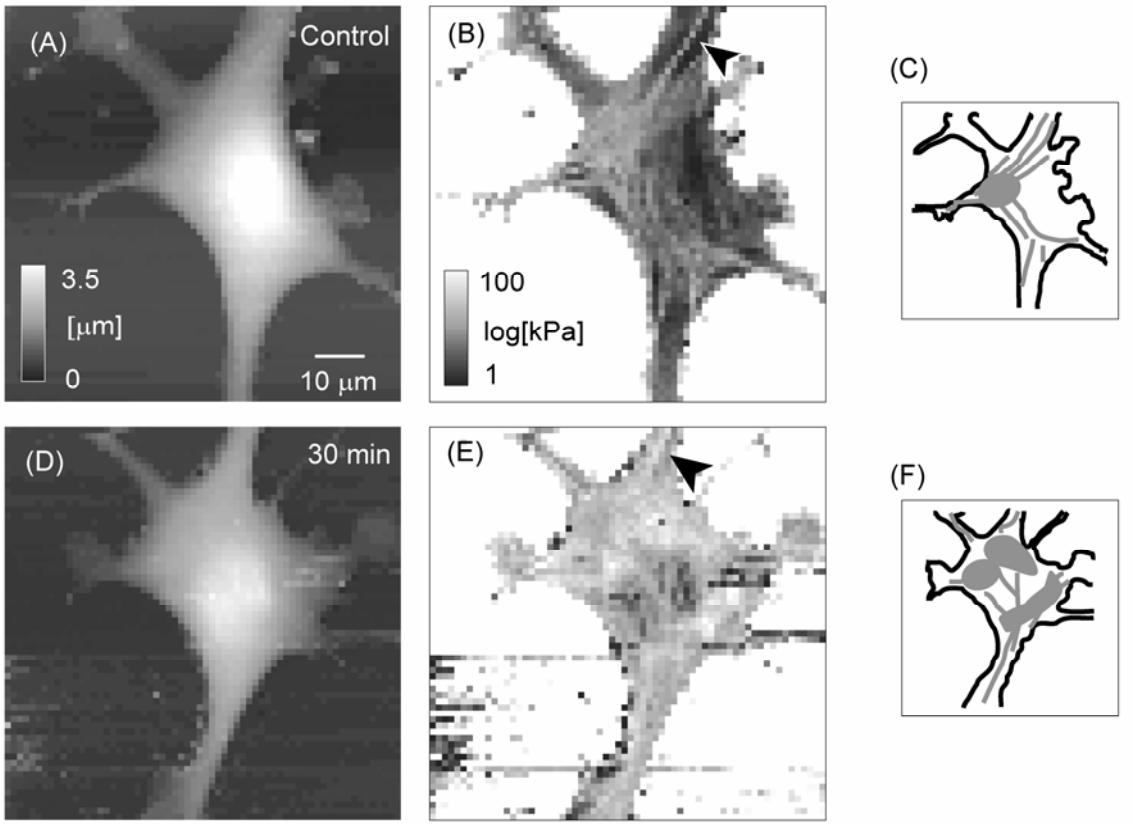

Figure 3.16 Topographic and stiffness images of a living fibroblast measured by force mapping mode before (A, B) and 30 min after stimulation by LPA (D, E), respectively. Schematic drawings (C, F) represent the distributions of stiff structures extracted from stiffness images (B, E).

Contrary to LPA, treatment with Y-27632 reduces cellular contractility. Figure 3.17 shows a variation in topographic and stiffness images of a fibroblast by treatment with Y-27632. These images are obtained by force mapping mode using type A cantilever. Figure (A) and (D) are topographic images before and 20 min after the treatment, respectively. The fibroblast treated with Y-27632 retracts partly and extends many small lamellipodia. Height of the fibroblast becomes about 0.3 μm higher. The round shape representing cell nucleus appears clearly on the surface. Figure (B) and (E) are stiffness images corresponding with the topographic images (A) and (D), respectively. Before treatment, many stress fibers appear clearly on cellular surface. The treatment with Y-27632 reduces stiffness of not only stress fibers (*arrow-heads*) but also whole of the cell. The softer region corresponding with cell nucleus seems to expand. Figure (C) and (F) show the distribution of stiff structures extracted from images (B) and (E). Although several stress fibers still remain, the treatment with Y-27632 makes two stiff

domains disappear. The same results are observed in all experimented cells without exception (n=4).

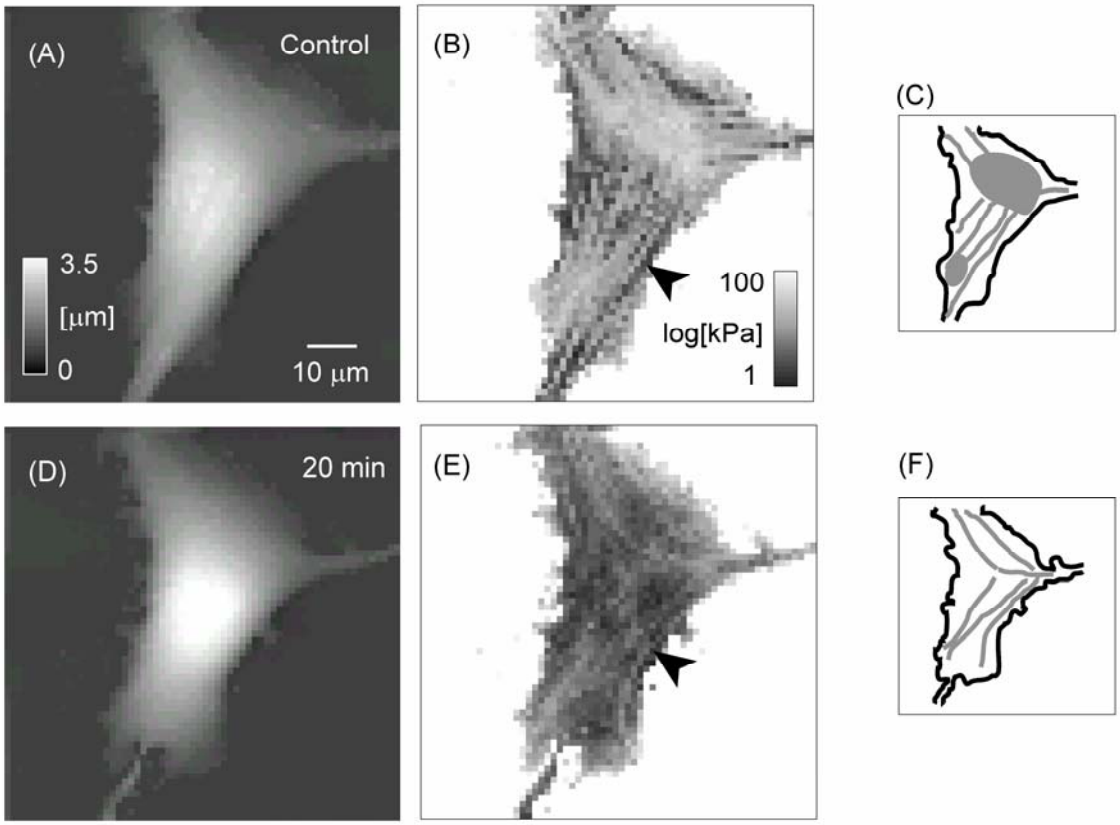

Figure 3.17 Topographic and stiffness images of a living fibroblast measured by force mapping mode before (A, B) and 20 min after treatment with Y-27632 (D, E), respectively. Schematic drawings (C, F) represent the distributions of stiff structures extracted from stiffness images (B, E).

3.5 Tensional coordination in cellular migration

As shown in Section 3.4, a cell varies its stiffness not locally but globally when its contractile force is regulated. The result suggests that stress fibers form contractile network covering the whole cell. The integrity and contractility of this network may give cells tensional coordination in cellular migration. In this section, a model of cellular migration based on tension is proposed. Then, a speculation about a spatial arrangement of stress fibers is described.

3.5.1 Network structures composed of stress fibers

In muscle cells, F-actin and myosin II form highly organized structure, called as myofibril, to generate large contractile force efficiently [6]. Figure 3.18 shows schematic drawing of the contractile structure. In the myofibril, bipolar filaments composed of many myosin II (~ 300 molecules) associating with antipallarel F-actin are regularly arranged every 2.2 μm. The repeating structure is connected to that of adjacent cells through a cell-cell contact. During muscle contraction, a directional movement of all myosin II on F-actin generates large contractile force. It is also widely known that temporary contractile filaments are formed in nonmuscle cells, especially fibroblasts. Although smaller and less highly organized, the contractile filaments resemble the tiny myofibrils in their structure and function. This is the reason that the contractile filament is called stress fiber. A direction of stress fibers running over dorsal surface of a cell corresponds with cellular polarity elongating highly to a direction of migration. A single stress fiber terminated at both anterior and posterior edges produces a contractile force polarized toward the direction of migration. When stress fibers lose scaffolds at the posterior edge, it shortens due to contractile force acting on itself. This leads to cellular migration dragging forward its posterior portion, and then the contractile force relaxes. In SPM measurements, stiffness is defined as a mechanical response to cantilever indentation. A tense stress fiber is stiffer than a relaxed one. This is consistent with the results that cellular stiffness decreases during migration and stiffness of a stress fiber varies with increase/decrease of its contractility.

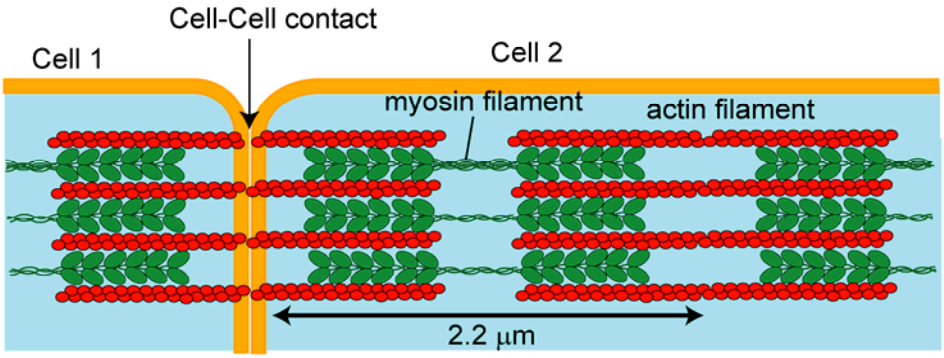

Figure 3.18 Schematic drawing of two muscle cells jointed end to end. Myofibrils in each cell are also jointed through cell-cell contact. Thus, the myofibrils continue across the muscle, ignoring cell boundaries.

Figure 3.19 shows magnified images of F-actin distribution, which is same image as shown in Figure 3.15. Many stress fibers run in parallel with cell polarity along three directions. The stress fibers are expected to be fixed on substratum through focal contacts only at each edge of the cell. Two regions including specific arrangement of stress fibers (*arrows*) are magnified. In the region indicated with ①, each stress fiber radiates in all directions from one point where it converges. In the region indicated with ②, one thick stress fiber branches off into two thinner ones toward cell body. Conversely, many stress fibers are bound into a thick bundle near a focal contact. These observations suggest that all stress fibers are connected each other and form contractile network covering the whole cell.

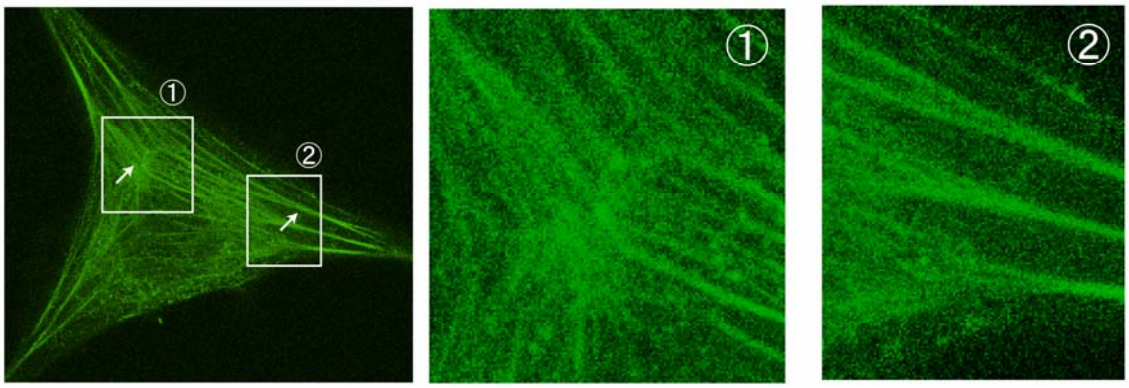

Figure 3.19 Distribution of F-actin obtained with CLSM (left). Two regions indicated with ① and ② in the left image are magnified (mid and right). These regions include specific arrangements (*arrows* in left) which suggest that all stress fibers are connected each other to form a network covering the whole cell.

3.5.2 Direction observations of temporal variation in focal contacts

Contractile force integrated over a whole cell can be regarded as tension. The tension leads to mechanical coordination in cellular migration. When the whole cell is integrated completely by tension, it is difficult that the cell extends a lamellipodium, moving focal contacts outward against its own tension. Focal contacts are considered to be formed newly after extension of lamellipodium. Focal contacts in a cultured fibroblast are observed with IRM described in Section 2.5. Figure 3.20(A) shows time-lapse images of a distribution of focal contacts during extension of lamellipodium. In these images, lamellipodium is extending (*arrow*) from an edge where some focal contacts exist (*oval*). During extension of lamellipodium, the focal contacts are completely stationary with reference to the substratum. This suggests that the lamellipodium can extend without being affected by an influence of tension that stress fiber generates. Figure 3.20(B) shows time-lapse images of new focal contacts after extension of lamellipodium. New focal contacts appear not on leading edge but inside lamellipodium (*oval*). This allows lamellipodium to extend continuously without an influence of tension. In these images, the existing focal contacts have two fates depending on its position as follows: A focal contact at the edge of the cell (*white arrow-head*) remains, but another inside the lamellipodium (*black arrow-head*) gradually disappears when new focal contacts are formed in the outer area. The tension

is expected to increase according to not lamellipodium extension but subsequent focal contacts formation. Time-lapse images of focal contacts in a retracting posterior portion are shown in Figure 3.20(C). Two focal contacts appear in the edge of the cell (*arrows*). They are moving toward cell body along with retraction of the edge (30 min), and finally disappear (60 min). The tension is expected to relax immediately after initiation of retraction of the posterior portion.

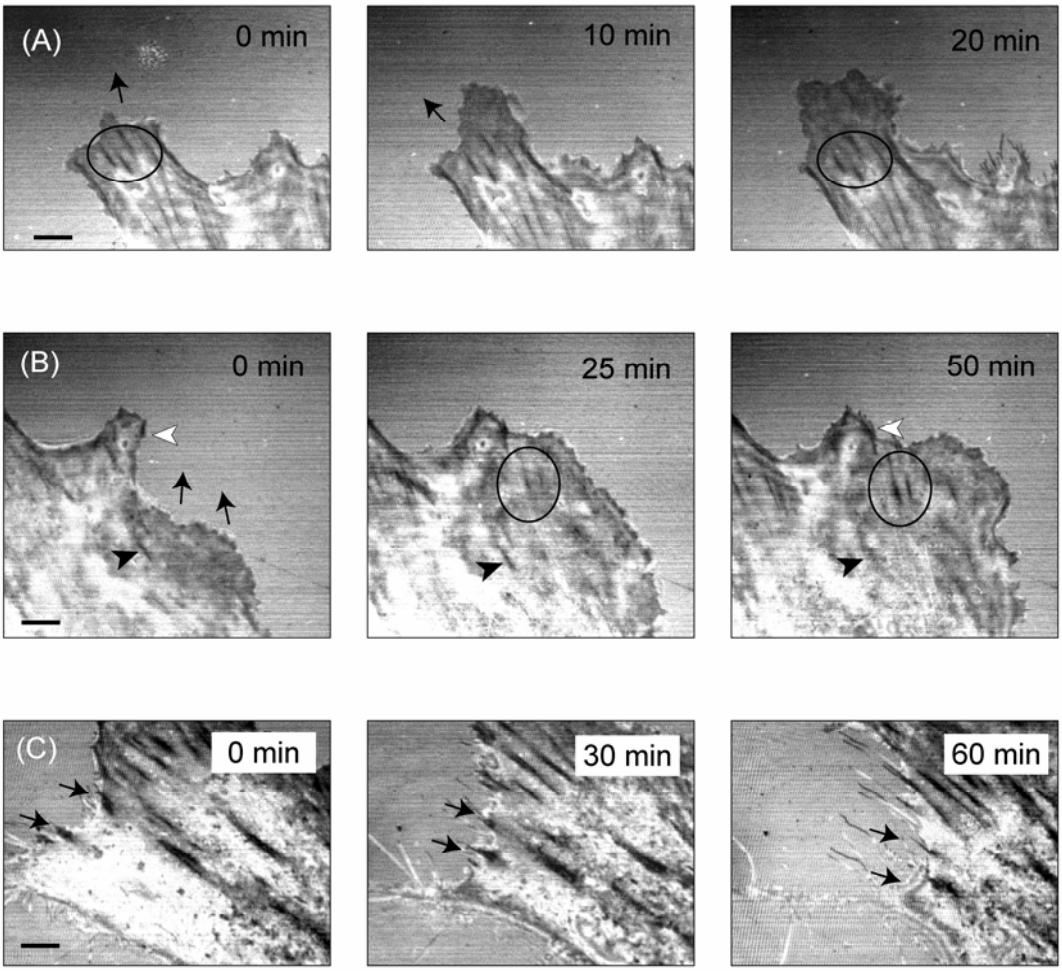

Figure 3.20 Time-lapse images of a distribution of focal contacts in cultured fibroblast obtained with IRM. Darker patches represent focal contacts. Scale bar, 5 μm. (A) During extension of lamellipodium, focal contacts (*oval*) are completely stationary. (B) New focal contacts are appearing inside the lamellipodium (*oval*). (C) Focal contacts (*arrows*) are moving along with retraction of the edge. Time intervals of three time-lapse series are 10 min (A), 25 min (B) and 30 min (C), respectively.

3.5.3 Model of tensional coordination in cellular migration

We propose a model as to how cells achieve one step of migration, as shown in Figure 3.21. Some mechanical or biochemical stimuli trigger off a cellular migration. When a cell receives local stimulations, it extends lamellipodia, and then forms new focal contacts to attach the lamellipodium to substratum (Stage 1). It has been reported that nascent focal contacts transmit stronger force to substratum than mature ones [42, 43]. When the cell begins to generate force at the new focal contacts in addition to the existing ones, cellular tension is increasing gradually (Stage 2). In other words, local extension is transmitted to the whole cell through the increase in tension. Cellular stiffness also increases gradually. Disassembly of focal contacts has been studied intensively at molecular level [44]. Mechanical stress loaded on cells weakens focal contacts through at least two signaling pathways: (i) Calpain as a protease is activated through a stretched-activated calcium channel (SA channel) [45-47]. (ii) Several proteins including focal adhesion kinase (FAK) and paxillin are bound to focal contacts through a deformation of cytoskeleton [48]. Consequently, increasing tension weakens focal contacts, and then detaches the weaker focal contacts (Stage 3). Cellular tension and stiffness reach maximum just before initiation of detaching focal contacts. Detachment of focal contacts at a portion of the cell induces retraction of the portion. This leads to cellular migration dragging cell body forward (Stage 4). At this time, the cellular tension relaxes and cellular stiffness drastically decreases due to the tension relaxation. An expected correlation between cellular stiffness and migration from the model is summarized in Figure 3.22(A). Cells are expected to repeat the change in its stiffness while they migrate. Figure 3.22(B) shows a relation between stiffness and migration measured by force modulation mode. Drastic decreasing in stiffness with migration corresponds exactly with a part ranging from Stage 3 to Stage 4 in the conceptual correlation (*grayed areas* in (A) and (B)). This correspondence supports strongly the present model. Cellular stiffness begins to increase again just after one step of migration. The increase in stiffness is expected to originate in an appearance of new stress fibers on cellular surface (see Figure 3.11). The appearance of stress fibers may suggest that extension of lamellipodium and formation of focal contacts occur continuously in the cell.

This model suggests that extension and retraction are coordinated mechanically by tension. According to the model, cellular migration is driven by balance between intracellular tension and extracellular adhesive force. In the recent works, it has been

reported that cellular migration is guided by not only chemical properties of ECM but also mechanical properties of substratum [49]. The tensional coordination in cellular migration may allow cells to orient and migrate in response to mechanical stimulus from the outside.

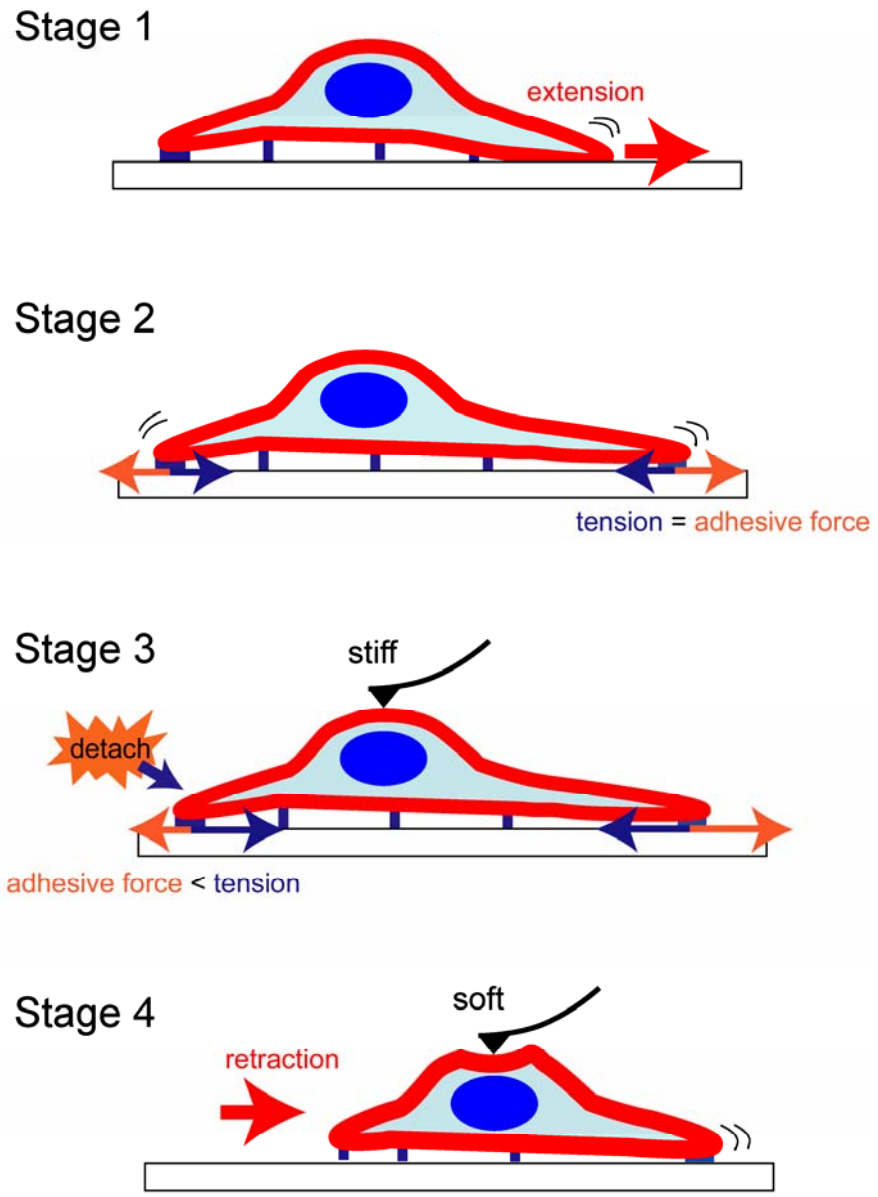

Figure 3.21 Tensional coordination in cellular migration. Stage 1: A cell extends lamellipodia, and then lamellipodia adheres to substratum. Stage 2: Formation of new focal contacts at the outside of the existing ones raises cellular tension. Stage 3: Increasing tension weakens focal adhesions, and overcomes adhesive force. Stage 4: Detachment of focal contact at a portion of the cell leads to cellular migration dragging cell body forward. At this time, cellular tension relaxes. Cellular tension acts as a mechanical coordination in cellular migration.

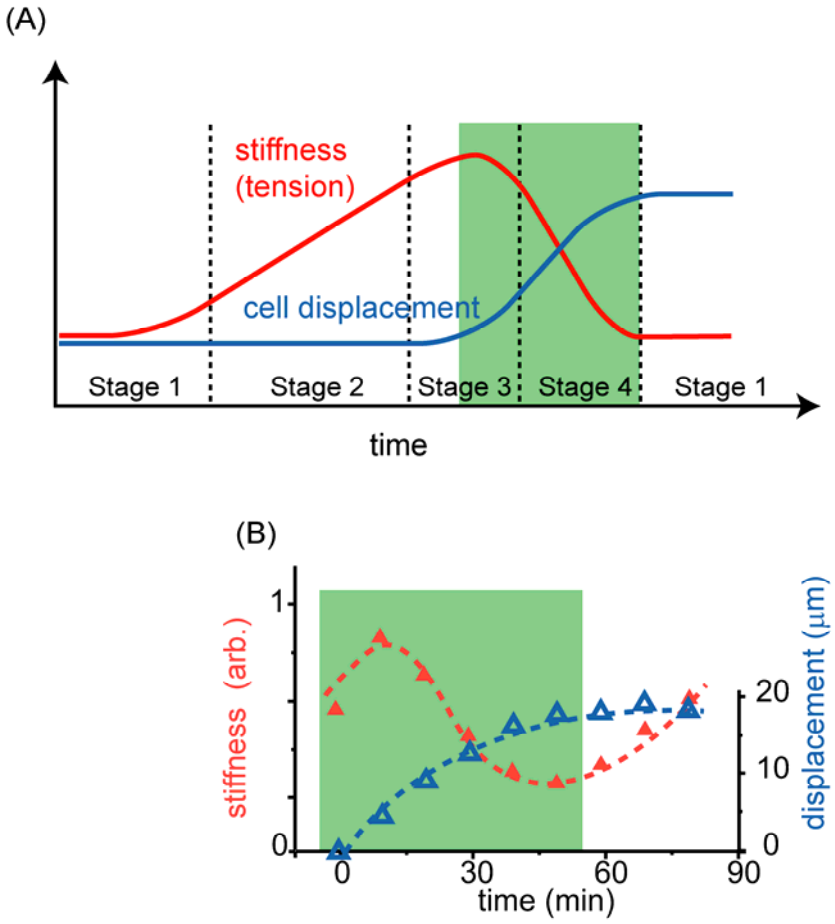

Figure 3.22 (A) Conceptual correlation between cellular stiffness and migration. Stage 1: Stiffness is almost constant. Stage 2: Stiffness gradually increases with forming new focal contacts. Stage 3: Stiffness reaches maximum just before initiation of focal contact disassembly. Stage 4: Stiffness drastically decreases due to tension relaxation caused by cell body contraction. In this stage, a cell migrates for one step. (B) Experimental correlation between cellular stiffness (*filled triangles*) and migration (*open triangles*) shown in Figure 3.14.

3.5.4 Further speculation about passive arrangement of stress fibers

We think that cellular tension plays essential role in arrangement of stress fibers. This speculation comes from a simple simulation shown in Figure 3.23. To demonstrate an arrangement of stress fibers, a two-dimensional meshwork made with elastic cords is

introduced (A). The meshwork mimicks contractile network structure. It is stretched and its three points are pinned to substratum by pushpins (B). The pushpins imitate focal contacts. When tension is supported with the pins discretely, the mesh is distorted due to own contractility. In respect to radial pattern, the anisotropic pattern appearing in the mesh is in good agreement with that of stress fibers in actual cells (C). Branches of elastic cord corresponding with those of stress fibers near the focal contact appear in this pattern, (*arrow* in (B)). Although it is widely known that focal contacts do not always exist tightly in periphery regions, an outline of cells shows not straight line but concave one (*arrow-head* in (C)). Surprisingly, this simple toy can reproduce typical cellular shape. The simulation using a simple toy is not theoretical but demonstrates that stress fibers in a cell can be arranged passively, depending on only tension and focal contact. In this process, no specific signaling molecules or actin-associated proteins, which have been believed to play critical roles, are necessary to arrange stress fibers. Thus, this gives a novel interpretation: An arrangement of stress fibers is formed passively due to anisotropic distortion of contractile network rather than it is formed actively for cellular migration.

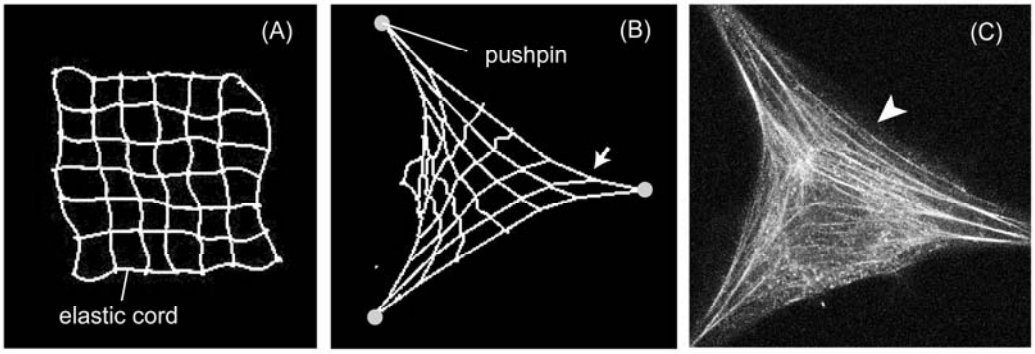

Figure 3.23 Two-dimensional meshwork is made with elastic cords, which mimics contractile network structure (A). When the stretched mesh is pinned at three points by the pushpins, the mesh shows a radial pattern (B). The radial pattern is in good agreement with that of stress fibers in an actual cell (C).

This speculation is supported partially by the following results. Figure 3.24 shows schematic drawings of an arrangement of stress fibers in two typical phase of cellular migration. (A) A migrating cell is highly polarized along one direction of migration (*arrows*). As shown in the insets, all stress fibers are in parallel and no stiff domain

appears. (B) On the other hand, a stationary cell has not linear shape. Stress fibers show a radial pattern with intersection points (*arrow-head*). As shown in the insets, the intersection points appear clearly as stiff domains on the cellular surface. These results are consistent with arrangements of stress fibers, expected from the speculation.

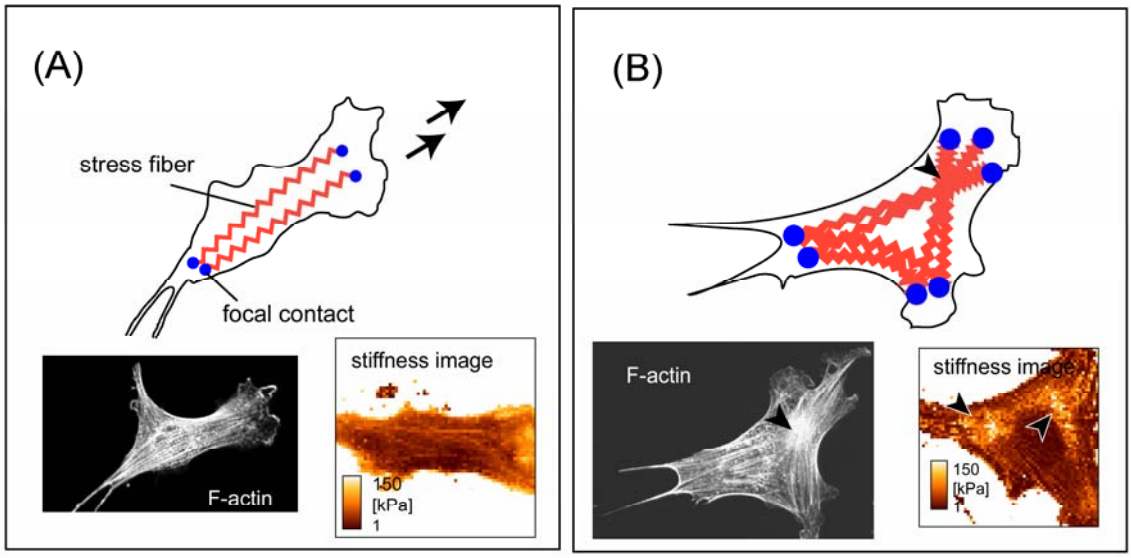

Figure 3.24 Schematic drawings an arrangement of stress fibers in typical migrating (A) and stationary cells (B). Insets in each schematic drawing are a distribution of F-actin and a stiffness image. These images are obtained with CLSM and SPM, respectively.

According to the simulation using contractile meshwork, increase in contractile force of elastic cords induces rearrangement of them. This can explain an appearance or disappearance of stiff domains when cellular contractility is regulated (described in 3.4.2). It is widely know that confluent cells stop proliferating (see Figure 1.1). According to the recent study, extension of cell on substratum is essential for adhesive cells to divide [50]. These suggest that the tensional coordination acts as a regulator for not only cellular migration but also proliferation. To prove our speculation, however, further critical experiments such as direct observation of rearrangement of stress fibers due to loading external force are still needed.

Chapter 4 Summary

Force modulation mode

Understanding cellular migration as an integrated mechanical system requires an experimental investigations on mechanical properties of living cells. Force modulation mode with SPM is proposed as a useful method for measuring stiffness of living cells with high temporal and spatial resolution. However, in liquid environment, cellular stiffness obtained by force modulation mode is often incredible. The following improvements are introduced in force modulation mode:

- A suitable frequency for measurement of viscoelasticity is selected according to frequency dependences of cantilever vibration.
- An instrument for operating at low frequency is built up.
- An analysis of SPM cantilever vibration is adopted.

Quantitative stiffness obtained by improved force modulation mode is verified as follows:

- Surface roughness does not affect stiffness data.
- Values of stiffness measured by this mode and force mapping mode show a linear relation.

As the result of above improvements and verifications, force modulation mode is established as a quantitative method for evaluating cellular stiffness in physiological conditions.

Cellular stiffness

Cellular stiffness of living fibroblasts is measured by improved force modulation mode or force mapping mode. A spatial and temporal distribution of cellular stiffness of fibroblasts is revealed. These results are summarized below:

- Spatial distribution of cellular stiffness is mainly attributed to network structures of F-actin.
- The structures give cells not rigid but contractile framework composed of F-actin associated with myosin II, namely, stress fiber.
- In a migrating cell, cellular stiffness drastically is decreasing when the cell is

migrating, and then, it begins to increase when the cell stops migrating.

- In a stationary cell, cellular stiffness is almost constant.
- Increase in cellular contractility raises stiffness of not only stress fibers but also whole of the cell.
- Increase in cellular contractility makes stiff domains appear on cellular surface.
- Decrease in cellular contractility reduces stiffness of not only stress fibers but also whole of the cell.
- Although several stress fibers still remain, decrease in cellular contractility makes stiff domains disappear.

These results suggest that a temporal variation of stiffness due to cellular migration originates in a variation of contractile force acting on network of stress fibers. Integrity of this contractile network is expected to give cells mechanical coordination in cellular migration.

Tensional coordination in cellular migration

A spatial arrangement of stress fibers and a temporal variation in focal contacts are observed in detail. These experiments are summarized below:

- Stress fibers are connected each other over the whole cell.
- When a lamellipodium extends, focal contacts are stationary with reference to substratum.
- After lamellipodium extension, new focal contacts appear inside the lamellipodium.
- When a portion of a cell retracts, focal contacts on the retracting edge move toward cell body and then disappear.

A following model of tensional coordination in cellular migration is proposed:

- Contractile force integrated over the whole cell acts as tension.
- Local extension is transmitted even to the opposite edges as an increase in tension.
- A single cell coordinates its extension and retraction mechanically by tension in cellular migration.
- Cellular migration is driven by balance between tension and adhesive force.

The tensional coordination gives a novel interpretation: An arrangement of stress fibers is formed passively due to anisotropic distortion of contractile network. To prove this speculation, further critical experiments are still needed.

Future prospects

The tensional coordination suggests that each cell behaves as a single mechanical system. The mechanical behavior is not confined to cellular migration. The mechanical coordination may act as a regulator for cellular proliferation. And furthermore, it may achieve not only intracellular but also intercellular communication through mechanical properties of substratum or ECM, besides chemicals. Thus, the present study on cellular behavior from mechanical viewpoints gives a major breakthrough in cancer biology and tissue engineering. Cellular migration is regarded as a macroscopic dynamics with a characteristic spatial and temporal scale in non-equilibrium systems. Living matters as non-equilibrium systems have hardly been investigated experimentally. In the near future, dynamics in non-equilibrium systems will be a hot subject in physics to approach macroscopic phenomena. Thus, the present study is a pioneer physics in living phenomena with flexibility and purposiveness.

Appendix

Effective mechanical properties of cantilever

When a cantilever is vibrated in liquid, drag force of the liquid influences cantilever vibration. Taking account into this influence, effective mass m^* and effective damping coefficient c^* are introduced in one-dimensional differential equation of the cantilever vibration as follows:

$$m^* \frac{\partial y^2(x,t)}{\partial t^2} + c^* \frac{\partial y(x,t)}{\partial t} + E_c I \frac{\partial y^4(x,t)}{\partial x^4} = p(x,t)$$

where $y(x,t)$ and $p(x,t)$ are deflection from a balanced position and loading force of the cantilever at position x ($0 \le x \le L$) and time t, respectively. L is the length of the cantilever. E_c and I are Young's modulus and geometrical moment of inertia, respectively. Inertia and damping components of the drag force are involved in m^* and c^*, respectively. In case of a rectangle cantilever, however, it is difficult to calculate values of m^* and c^* theoretically. So a cylinder whose diameter is equal to width of the cantilever is considered, as shown in Figure A.1.

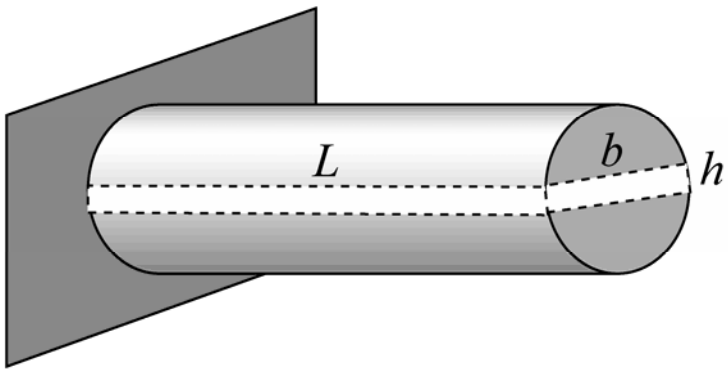

Figure A.1 Cylinder model. A rectangle cantilever with length of L, width of b and thickness of h is assumed to be a cylinder with diameter of b.

On the assumption that the drag force loaded on the rectangle cantilever are equivalent to that of the cylinder, m^* and c^* of the rectangle cantilever when it is vibrated in liquid can be expressed as follows [51, 52]:

$$m^* = \rho_b bh + k\pi\rho b^2$$
$$c^* = k'\omega\pi\rho b^2$$

where b, ρ_b and h are the width, density and thickness of the cantilever, respectively. ω represents angular frequency of the cantilever vibration. ρ is density of the liquid. Non-dimensional k and k' are expressed as follows:

$$k - ik' = 1 + \frac{4iK_1(-i\sqrt{iR_e})}{\sqrt{iR_e}K_0(-i\sqrt{iR_e})}$$

where, K_0 and K_1 are modified Bessel function, and R_e is Reynolds number ($= \rho\omega b^2/(4\mu)$). μ is coefficient of viscosity of the liquid. i represents imaginary unit. In the present study, m^* and c^* estimated by the cylinder model, mentioned above, are adopted.

Steady state solutions to equation on cantilever vibration

When external vibration is applied to sample stage, one-dimensional differential equation on a vibration of cantilever attached at its end to a viscoelastic sample is given as follows (see 3.1.3):

$$m^*\frac{\partial y^2(x,t)}{\partial t^2} + c^*\frac{\partial y(x,t)}{\partial t} + E_c I\frac{\partial y^4(x,t)}{\partial x^4}$$
$$= -\left[K_s\{\phi(t) - y(L,t)\} + C_s\frac{\partial\{\phi(t) - y(L,t)\}}{\partial t}\right]\delta(x-L)$$

where, K_s [N/m] and C_s [N·s/m] are one-dimensional surface elasticity and viscosity of the sample, respectively. $\phi(t)$ is a vibration applied to the sample externally. $\delta(x)$ is Dirac delta function and other parameters. The first mode vibration is expected to be dominant in the cantilever deflection $y(L,t)$ since the deflection due to higher mode vibration is much smaller than that of the first mode. Under this assumption, steady state solutions to the above equation can be obtained as follows:

$$y(L,t)/a = W(\omega)\cdot\exp(i\omega t)$$

where, a and ω are amplitude and angular frequency of applied external vibration to stage, respectively. $W(\omega)$ is non-dimensional amplitude expressed as follows:

$$W(\omega) = Y_1(L)\frac{(\frac{K_s}{4K} + i\frac{2C_s}{C_c}\frac{\omega}{\omega_1})Y_1(L)}{\left[1+\frac{K_s}{4K}\{Y_1(L)\}^2\right] - \frac{\omega^2}{{\omega_1}^2} + 2i\frac{\omega}{\omega_1}\left[\frac{C}{C_c}+\frac{C_s}{C_c}\{Y_1(L)\}^2\right]}$$

where,

$K(\text{stiffness of cantilever}) = 1.875^4 E_c I/L,$

$C = c^* L, \quad C_c = 2m^* L\omega_1, \quad {\omega_1}^2 = (E_c I/m^*){k_1}^4, \quad k_1 = 1.875/L,$

$Y_1 = \cosh k_1 L - \cos k_1 L - K_1(\sinh k_1 L - \sin k_1 L),$

$K_1 = (\cosh k_1 L + \cos k_1 L)/(\sinh k_1 L + \sin k_1 L).$

Using the real α and imaginary part β of $W(\omega)$, amplitude ratio A and phase shift θ of the cantilever vibration can be expressed as follows:

$$W(\omega) = \alpha(K_s, C_s) + i\beta(K_s, C_s)$$

$$A = |W(\omega)| = \sqrt{\alpha^2+\beta^2}$$

$$\theta = -\tan^{-1}(\beta/\alpha)$$

where, α and β are functions of both K_s and C_s. This means that a A and θ can be evaluated when a K_s and C_s are given. Figure A.2 shows a relation between the sample viscoelasticity (K_s, C_s) and the cantilever vibration (A, θ). In force modulation mode, A and θ are measured directly by photo detector. Fitting to map of the theoretical relation, quantitative K_s and C_s are evaluated from experimental A and θ.

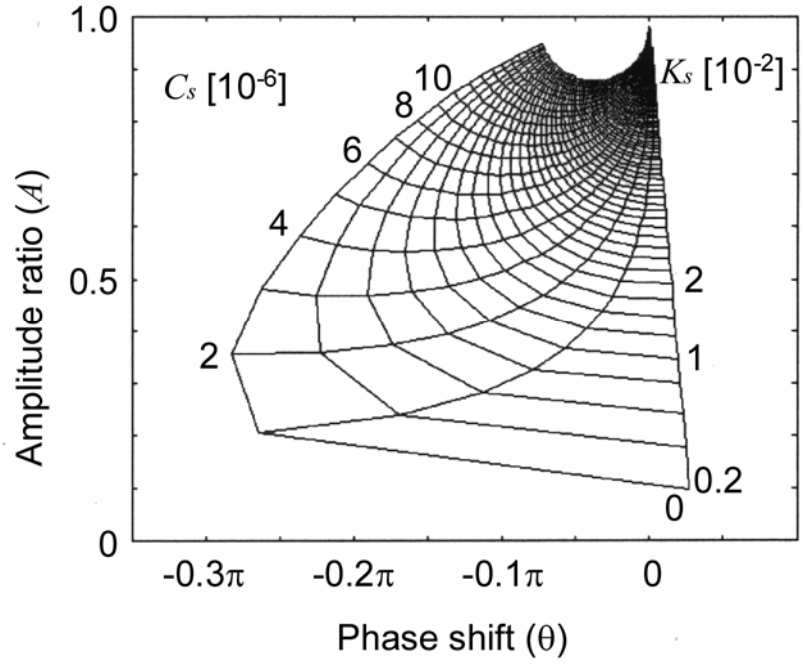

Figure A.2 Map of relation between the sample viscoelasticity (K_s, C_s) and the cantilever vibration (A, θ). Angular frequency ω applied to sample stage is 500 Hz.

Calculation of Young's modulus and coefficient of viscosity

On the assumption viscoelastic response of a sample obeys Voigt model, resistance force p^* of a sample against sinusoidal indentation (amplitude d, angular frequency ω) is expressed as follows:

$$p^* = (K_s + i\omega C_s)d$$

When the sinusoidal indentation d is superimposed on pre-indentaion d_o ($\gg d$), Sneddon model should be modified by using complex Young's modulus E^* ($= E + i\omega\eta$) as follows:

$$P^* = AE^*(d_0 + d)^2$$
$$A = \frac{2\tan\alpha}{\pi(1-\nu^2)}$$

where, P^* is net resistance force of a sample. P^* can be separated into two components induced by pre-indentation d_o and sinusoidal indentation d, respectively. These components indicated with p_0 and p^* correspond with terms of $d_o{}^2$ and $d_o \cdot d$ on the above equation. These are expressed as follows:

$$p_0 = AEd_0{}^2$$
$$p^* = 2AE^* d_0 \cdot d = 2\sqrt{\frac{Ap_0}{E}}(E + i\omega\eta)d$$

where, E^* in the equation of p_0 is equal to E since p_0 is constant independently of time. The term of d^2 can be ignored because of $d_o \gg d$. The above two equations of p^* (K_s, C_s) and p^* (E, η) allow to calculate Young's modulus E [Pa] and coefficient of viscosity η [Pa·s] from one-dimensional elasticity K_s and viscosity C_s of a sample. The formulas are expressed as follows:

$$E = \frac{\pi(1-\nu^2)}{8p_0 \tan\alpha} K_s{}^2, \qquad \eta = \frac{\pi(1-\nu^2)}{8p_0 \tan\alpha} K_s C_s$$

References

[1] http://expmed.bwh.harvard.edu/projects/motility/neutrophil.html

[2] Czirók, A., Schlett, K., Madarász, E. and Vicsek, T. *Phys. Rev. Lett.* **81(14)**, 3038-3041 (1998).

[3] Lauffenburger, D. A. and Horwitz, A. F. *Cell* **84(3)**, 359-369 (1996).

[4] Horwitz, A. R. and Parsons, J. T. *Science* **286(5442)**, 1172-1174 (1999).

[5] Bray, D. *Cell Movements: from Molecules to Motility*, 2nd ed., Garland Publishing, New York (2001).

[6] Alberts, B., Johnson, A., Lewis, J., Raff, M., Roberts, K. and Walter, P. *Molecular Biology of the Cell*, 4th ed., Garland Publishing, New York (2002).

[7] Waterman-Storer, C. M. and Salmon, E. D. *Curr. Opin. Cell Biol.* **11(1)**, 61-67 (1999).

[8] Waterman-Storer, C. M., Worthylake, R. A., Liu, B. P., Burridge, K. and Salmon, E. D. *Nat. Cell Biol.* **1(1)**, 45-50 (1999).

[9] van Leeuwen, F. N., van Delft, S., Kain, H. E., van der Kammen, R. A. and Collard, J. G. *Nat. Cell Biol.* **1(4)**, 242-248 (1999).

[10] Symons, M. and Settleman, J. *Trends Cell Biol.* **10(10)**, 415-419 (2000).

[11] Ridley, A. J. *J. Cell Sci.* **114**, 2713-2722 (2001).

[12] Harris, A. K., Wild, P. and Stopak, D. *Science* **208**, 177-180 (1980).

[13] Ingber, D. E. *J. Cell Sci.* **104**, 613-627 (1993).

[14] Ingber, D. E. *Annu. Rev. Physiol.* **59**, 575-599 (1997).

[15] Ingber, D. E. *J. Cell Sci.* **116(7)**, 1157-1173 (2003).

[16] Ingber, D. E. *J. Cell Sci.* **116(8)**, 1397-1408 (2003).

[17] Dembo, M. and Wang, Y. -L. *Biophys. J.* **76**, 2307-2316 (1999).

[18] Munevar, S., Wang, Y. -L. and Dembo, M. *Biophys. J.* **80**, 1744-1757 (2001).

[19] Munevar, S., Wang, Y. -L. and Dembo, M. *Mol. Biol. Cell* **12(12)**, 3947-3954 (2001).

[20] Peterson, N. O., McConnaughey, W. B. and Elson, E. L. *Proc. Natl. Acad. Sci. USA* **79**, 5327-5331 (1982).

[21] Zaharak, G. I., McConnaughey, W. B. and Elson, E. L. *J. Biomech. Eng.* **112**, 283-294 (1990).

[22] Evans, E., Ritchie, K. and Merkel, R. *Biophys. J.* **68**, 2580-2587 (1995).

[23] Shao, J. -Y. and Hochmuth, R. M. *Biophys. J.* **71**, 2892-2901 (1996).

[24] Ashkin, A. and Dziedzic, J. M. *Proc. Natl. Acad. Sci. USA* **86**, 7914-7918 (1989).

[25] Svoboda, K., Schmidt, C. F., Branton, D. and Block, S. M. *Biophys. J.* **63**, 784-793 (1992).

[26] Henon, S., Lenormand, G., Richert, A. and Gallet, F. *Biophys. J.* **76**, 1145-1151 (1999).

[27] Bausch, A. R., Ziemann, F., Boulbitch, A. A., Jacobson, K. and Sackmann, E. *Biophys. J.* **75**, 2038-2049 (1998).

[28] Bausch, A. R., Moller, W. and Sackmann, E. *Biophys. J.* **76**, 573-579 (1999).

[29] Wang, N. and Stamenovic, D. *Am. J. Physiol. Cell Physiol.* **279**, C188-C194 (2000).

[30] Binnig, G., Quate, C. F. and Gerber, C. *Phys. Rev. Lett.* **56**, 930-933 (1986).

[31] Radmacher, M., Fritz, M., Kacher, C. M., Cleveland, J. P. and Hansma, P. K. *Biophys. J.* **70**, 556-567 (1996).

[32] Radmacher, M., Tillmann, R. W., Fritz, M. and Gaub, H. E. *Science* **257**, 1900-1905 (1992).

[33] Radmacher, M., Tillmann, R. W. and Gaub, H. E. *Biophys. J.* **64**, 735-742 (1993).

[34] Hertz, H. *J. Reine Angew. Math.* **92**, 156-171 (1881).

[35] Sneddon, I. N. *Fourier Transforms*, McGraw Hill Book Company, Inc., New York (1951).

[36] Somlyo, A. P. and Somlyo, A. V. *J. Physiol.* **522.Pt 2**, 177-185 (2000).

[37] Parizi, M., Howard, E. W. and Tomasek, J. J. *Exp. Cell Res.* **254**, 210-220 (2000).

[38] Deng, J. T., Van Lierop, J. E., Sutherland, C. and Walsh, M. P. *J. Biol. Chem.* **276(19)**, 16365-16373 (2001).

[39] Curtis, A. S. G. *J. Cell Biol.* **20**, 199-215 (1964).

[40] Abercrombie, M. and Dunn, G. A. *Exp. Cell Res.* **92**, 57-62 (1975).

[41] Opas, M. *Proc.Int.Soc.Opt.Eng.* **SPIEE 1121**, 351-356 (1990).

[42] Beningo, K. A., Dembo, M., Kaverina, I., Small, J. V. and Wang, Y. -L. *J. Cell Biol.* **153(4)**, 881-887 (2001).

[43] Galbraith, C. G., Yamada, K. M. and Sheetz, M. P. *J. Cell Biol.* **159(4)**, 695-705 (2002).

[44] Webb, D. J., Parsons, J. T. and Horwitz, A. F. *Nat. Cell Biol.* **4(4)**, E97-100 (2002).

[45] Palecek, S. P., Huttenlocher, A., Horwitz, A. F. and Lauffenburger, D. A. *J. Cell Sci.* **111(Pt 7)**, 929-940 (1998).

[46] Lee, J., Ishihara, A., Oxford, G., Johnson, B. and Jacobson, K. *Nature* **400(6742)**, 382-386 (1999).

[47] Charras, G. T. and Horton, M. A. *Biophys. J.* **82(6)**, 2970-2981 (2002).

[48] Sawada, Y. and Sheetz, M. P. *J. Cell Biol.* **156(4)**, 609-615 (2002).

[49] Lo, C. -M., Wang, H. -B., Dembo, M. and Wang, Y. -L. *Biophys. J.* **79(1)**, 144-152 (2000).

[50] Huang, S. and Ingber, D. E. *Nat. Cell Biol.* **1(5)**, E131-138 (1999).

[51] Tuck, E. O. *J. Eng. Math.* **3**, 29-44 (1969).

[52] Sader, J. E. *J. Appl. Phys.* **84**, 64-76 (1998).

Acknowledgements

I would like to express my sincere gratitude to Professor Kazushige Kawabata, Professor Hisashi Haga and for the continuous guidance and encouragement they has provided throughout the present study. I am grateful to Professor Masayuki Ido and Professor Koji Nemoto for their valuable comments and critical reading of this dissertation manuscript.

We collaborated with Professor Yoshio Tanaka, Professor Yoshihiko Hirai, Mr. Masaaki Kabuto and Mr. Keiji Yamauchi of Osaka Prefecture University in establishing quantitative force modulation mode (described in Section 3.1 and Appendix). I would like to express my gratitude to the collaborators for their computer simulation and helpful discussion.

I am grateful to Professor Etsuro Ito and his Lab members for their biological suggestion. I gratefully appreciate the biochemical advice from Professor Masayuki Takahashi and his Lab members. I am grateful to Professor Masaharu Tokunaga, Professor Toshirou Yagi and Professor Tadanao Ito for their valuable comments. I would like also to thank Professor Takashi Sambongi and past/present members of our Lab for their supports and encouragement.

Finally I would like to thank my family and all of my friends.